Multifunctional Cell-Culture Platform for Aligned Cell Sheet Monitoring, Transfer Printing, and Therapy

Seok Joo Kim,[†,‡,#] Hye Rim Cho,[†,§,#] Kyoung Won Cho,[†,‡,#] Shutao Qiao,[⊥] Jung Soo Rhim,[∥] Min Soh,[†,‡] Taeho Kim,[†,‡] Moon Kee Choi,[†,‡] Changsoon Choi,[†,‡] Inhyuk Park,[†,‡] Nathaniel S. Hwang,[‡] Taeghwan Hyeon,[†,‡] Seung Hong Choi,[*,†,§] Nanshu Lu,[*,⊥] and Dae-Hyeong Kim[*,†,‡]

[†]Center for Nanoparticle Research, Institute for Basic Science (IBS), Seoul 151-742, Republic of Korea, [‡]School of Chemical and Biological Engineering, Institute of Chemical Processes, Seoul National University, Seoul 151-742, Republic of Korea, [§]Department of Radiology, Seoul National University College of Medicine, Seoul 110-744, Republic of Korea, [⊥]Center for Mechanics of Solids, Structures, and Materials, Department of Aerospace Engineering and Engineering Mechanics, Texas Materials Institute, University of Texas at Austin, 210 E. 24th Street, Austin, Texas 78712, United States, and [∥]School of Mechanical and Aerospace Engineering, Seoul National University, Seoul 151-742, Republic of Korea. [#]S. J. Kim, H. R. Cho, and K. W. Cho contributed equally to this work.

ABSTRACT While several functional platforms for cell culturing have been proposed for cell sheet engineering, a soft integrated system enabling *in vitro* physiological monitoring of aligned cells prior to their *in vivo* applications in tissue regeneration has not been reported. Here, we present a multifunctional, soft cell-culture platform equipped with ultrathin stretchable nanomembrane sensors and graphene-nanoribbon cell aligners, whose system modulus is matched with target tissues. This multifunctional platform is capable of aligning plated cells and *in situ* monitoring of cellular physiological characteristics during proliferation and differentiation. In addition, it is successfully applied as an *in vitro* muscle-on-a-chip testing platform. Finally, a simple but high-yield transfer printing mechanism is proposed to deliver cell sheets for scaffold-free, localized cell therapy *in vivo*. The muscle-mimicking stiffness of the platform allows the high-yield transfer printing of multiple cell sheets and results in successful therapies in diseased animal models. Expansion of current results to stem cells will provide unique opportunities for emerging classes of tissue engineering and cell therapy technologies.

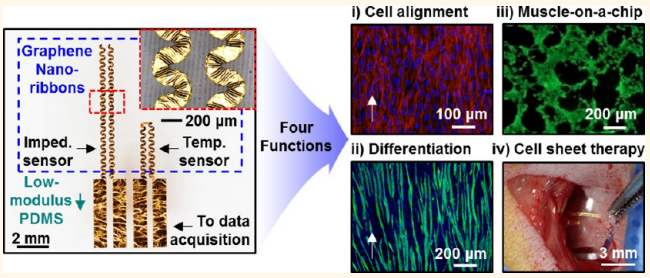

KEYWORDS: graphene nanoribbon · flexible nanomembrane electronics · cell alignment · real-time monitoring · ceria nanoparticle · transfer printing · regenerative medicine

Tissue engineering scaffolds, including two-dimensional cell-culture substrates, serve as synthetic extracellular matrices (ECMs) to support cells in culture systems and to assist the regeneration of damaged tissues.[1] Although significant progress in scaffold technology has been made,[2,3] including improvements in materials and structural designs, most scaffolds remain passive; that is, they provide only structural support without any *in situ* and real-time monitoring capability. Passive scaffolds thus need *ex situ* biological assays, which demands delicate assay techniques and the sacrifice of cells. Therefore, the development of active scaffolds embedded with sensors[4] that continuously monitor cellular physiology *in vitro* and the therapeutic application of cells prepared from such scaffolds *in vivo* represent a new frontier of tissue engineering. Wafer-based electronics have demonstrated such capabilities;[5] however, these rigid, planar wafers are mechanically incompatible with soft, flexible tissues. Toward this purpose, flexible[6,7] and stretchable[8−12] electronics offer a viable solution.

Meanwhile, biodegradability and cytotoxicity of onboard electronic devices may hinder the potential *in vivo* implantation of such electronic scaffolds. Scaffold-free cell sheet application is an attractive approach to overcome these limitations. Cell sheet therapy provides robust benefits in localized treatments by eliciting high paracrine effects and has been successfully used in the cornea,[13] periodontium,[14] and heart.[15] A temperature-sensitive polymer,

* Address correspondence to D.-H. Kim (dkim98@snu.ac.kr), N. Lu (nanshulu@utexas.edu), S. H. Choi (verocay@snuh.org).

Received for review November 12, 2014 and accepted February 16, 2015.

Published online 10.1021/nn5064634

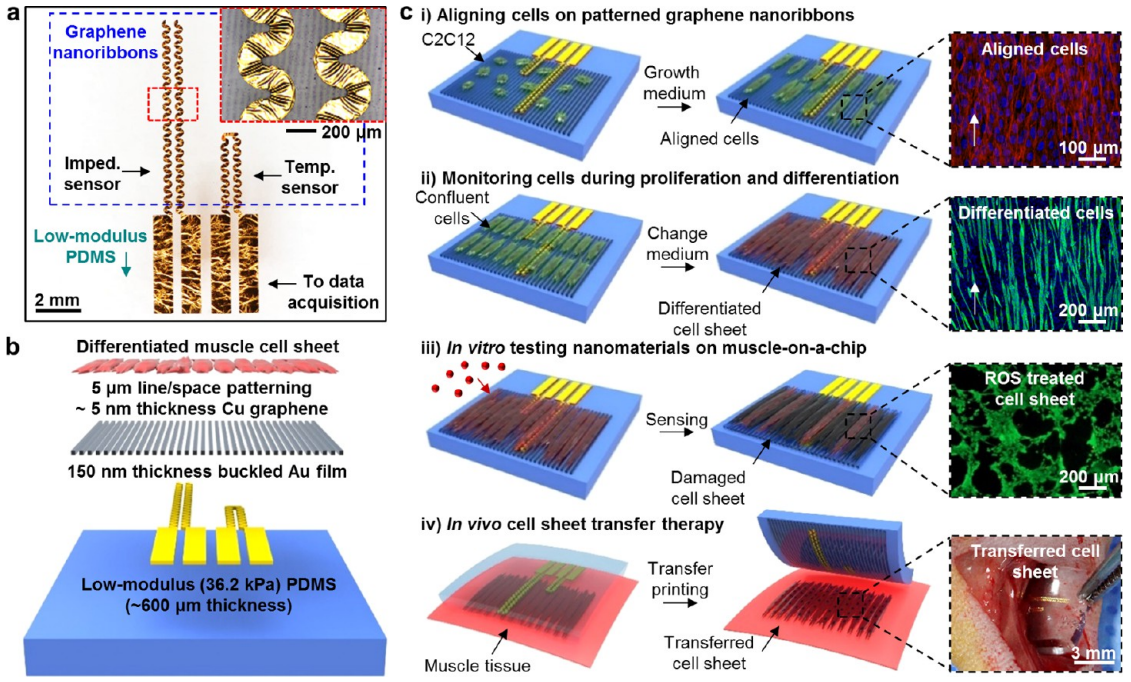

Figure 1. Overview of the architecture and key applications of the soft instrumented cell-culture platform. (a) The cell-culture platform is made of patterned graphene nanoribbons (top layer) and Au nanomembrane impedance/temperature sensors (bottom layer) on a low-modulus PDMS sheet. The top right inset shows the magnified view of serpentine-shaped buckled Au electrodes. (b) Expanded view of each element of the cell-culture platform. (c) Summary of the four key applications of the soft instrumented cell-culture platform: (i) aligning C2C12 myoblasts, (ii) *in situ* monitoring of proliferation and differentiation, (iii) evaluating the effects of novel nanomaterials and drugs *in vitro*, and (iv) transfer printing cultured cell sheets onto target sites of animal models *in vivo*.

poly(*N*-isopropylacrylamide) (PIPAAm), has been widely used to prepare and transfer cell sheets[13−15] to *in vivo* models. However, the electron irradiation process required to precisely control the ultrathin thickness (<30 nm) of the PIPAAm substrate[16] is highly delicate. Moreover, integrating PIPAAm with high-performance electronics is difficult because of its instability during the fabrication process of electronics (heat, solvent, acid, etching, *etc.*). Therefore, a simpler yet more electrically and mechanically engineered platform for scaffold-free cell sheet treatment is needed.

Here, we introduce a soft instrumented cell-culture platform composed of ultrathin stretchable gold nanomembrane sensors and patterned graphene-nanoribbon cell aligners on a biocompatible low-modulus (~36.2 kPa) polydimethylsiloxane (PDMS) substrate (Figure 1a,b). The low-modulus PDMS offers optimal softness that is compatible with native skeletal muscle tissues.[17] Stretchable physiology (impedance and temperature) sensors based on serpentine,[9,18] buckled[19−21] gold nanomembranes (Figure 1a inset) are fabricated using photolithography (Figure S1a in the Supporting Information). Anisotropically micropatterned (~5 μm lines and spaces; Figure S1b in the Supporting Information) graphene nanoribbons promote cell adhesion,[22,23] alignment,[24] and differentiation.[25] Ultrathin thicknesses of gold nanomembranes and graphene nanoribbons (~150 and ~5 nm, respectively) minimize the increase of the system modulus (44.9 kPa, integrated system), which is designed to be matched with target tissues (45.9 kPa, muscle). Intrinsically soft graphenes[12,26] also contribute low system modulus. The system modulus comparison between the instrumented platform and the muscle tissue is shown in Figure S2 in the Supporting Information. This soft instrumented cell-culture platform has four major functions (Figure 1c): (i) aligning cells on patterned graphene nanoribbons to promote muscle cell differentiation, (ii) real-time physiological monitoring of cells during proliferation and differentiation by integrated sensors, (iii) serving as an *in vitro* muscle-on-a-chip[27−29] platform to test the effects of novel nanomaterials or drugs, and (iv) *in vivo* transfer printing of differentiated cell layers for scaffold-free cell sheet treatments.

RESULTS

Aligning Cells on the Patterned Graphene Nanoribbons. Figure 2 presents details of cell alignment by applying the patterned graphene nanoribbons to a tissue-engineering platform. The graphene nanoribbons are transferred[26] on a low-modulus PDMS substrate. The sheet resistance is approximately 1 kΩ/sq (measured using a 4-point probe system; CMT-100MP, Advanced Instrument Technology). The atomic force microscopy (AFM) topological images and water contact angle of graphene nanoribbons (approximately 112.38°) are shown in Figure S3a−c in the Supporting Information. The $\pi-\pi$ interaction and hydrophobicity

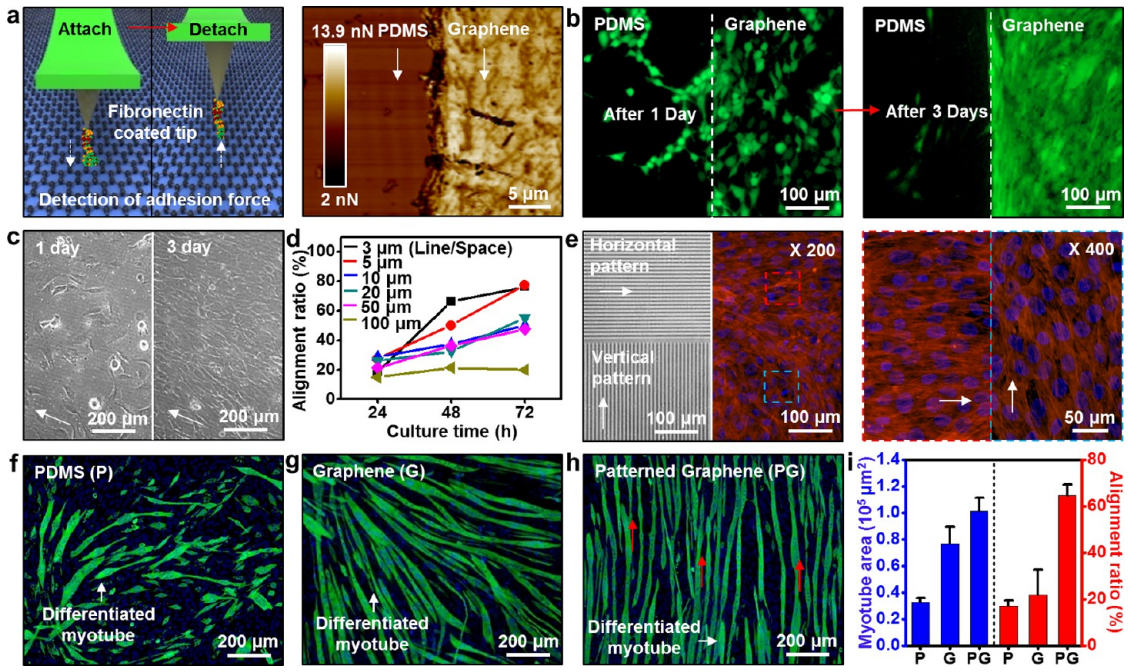

Figure 2. Alignment of the C2C12 myoblasts during proliferation and differentiation on the patterned graphene nanoribbons. (a) Measurement of the adhesion force between fibronectin molecules and graphene. The left frame shows a schematic illustration of AFM adhesion force measurements using the fibronectin-coated AFM tip, and the right frame presents the force map. (b) Images showing the biocompatible, cell-friendly surface of patterned graphene nanoribbons. (c) Images of aligned C2C12 myoblasts on the patterned graphene nanoribbons (~5 μm widths of both lines and spaces). (d) Cell alignment ratio as a function of culture time for different graphene feature sizes. The smaller feature size (~5 μm widths of both lines and spaces) yields a better alignment than the larger feature size. (e) Cell alignment on patterned graphene where horizontal (top) and vertical (bottom) patterns coexist (left frame), and magnified images of red- and blue-dotted boxed regions (right frame). (f–h) Myotube formation through myogenic differentiation after 7 days of culture on different substrates, including PDMS (P), graphene (G), and patterned graphene (PG). The red arrows indicate the direction of myotube alignment. (i) Plot of the myotube areas and alignment ratios on different substrates.

of the graphene[30] result in 6-fold stronger protein adhesion than PDMS alone, as shown in the AFM analysis, in which a fibronectin-coated tip is used (Figure 2a). The strongly adhesive properties of ECM proteins on graphene facilitate the cell adhesion.[31] Three days after culture, C2C12 myoblasts are preferably adhered and proliferated on the graphene nanoribbons without additional treatments (Figure 2b; fluorescence microscopic images, stained with calcein AM).

The widths and spacing of graphene nanoribbons are important for cell alignment. We cultured C2C12 myoblasts for 3 days on graphene-nanoribbon substrates with different feature sizes (Figure S4 in the Supporting Information). Phase-contrast microscopy is utilized to monitor cell alignment during the culture (Figure 2c; results of real-time monitoring by confocal microscopy is shown in video 1 in the Supporting Information). Cells are considered to be aligned along graphene-nanoribbon patterns when the cell orientation is within the range of $-10°$ to $+10°$ with respect to the ribbon orientation. Graphene patterns with nanoribbon widths and spacing of $<\sim 5$ μm show higher alignment ratios than those of 10–50 μm, while those of 100 μm show almost no alignment (Figure 2d). Figure 2e shows the cell alignment on graphene nanoribbons in which horizontal (top) and vertical (bottom) patterns are adjacent to each other. Right frame shows its magnified view. C2C12 myoblast differentiation is enhanced by patterned graphene nanoribbons as indicated by myosin heavy chain (MHC) immunostaining (Figure 2f–h).[32] C2C12 myoblasts exhibit larger myotube area and higher alignment ratio when grown on patterned graphene (Figure 2i) than those grown on bare PDMS or non-patterned graphene.

Physiological Monitoring during Proliferation and Differentiation. Impedance and temperature sensors are also integrated on the low-modulus PDMS substrate, but beneath the patterned graphene nanoribbons, allowing for the *in situ* and real-time monitoring of cellular activities (Figure 3a). Cell proliferation and differentiation alter the electrochemical environment around electrodes, and these changes can be detected as impedance or conductance changes.[33] For the impedance sensor, the alternating current (AC) flows through the culture medium between two serpentine electrodes spaced 600 μm apart. For the temperature sensor, we used a resistance temperature detector (RTD)[34] based on a serpentine gold nanomembrane. Figure 3b–d display the calibration curves of the temperature, impedance, and conductance sensors.

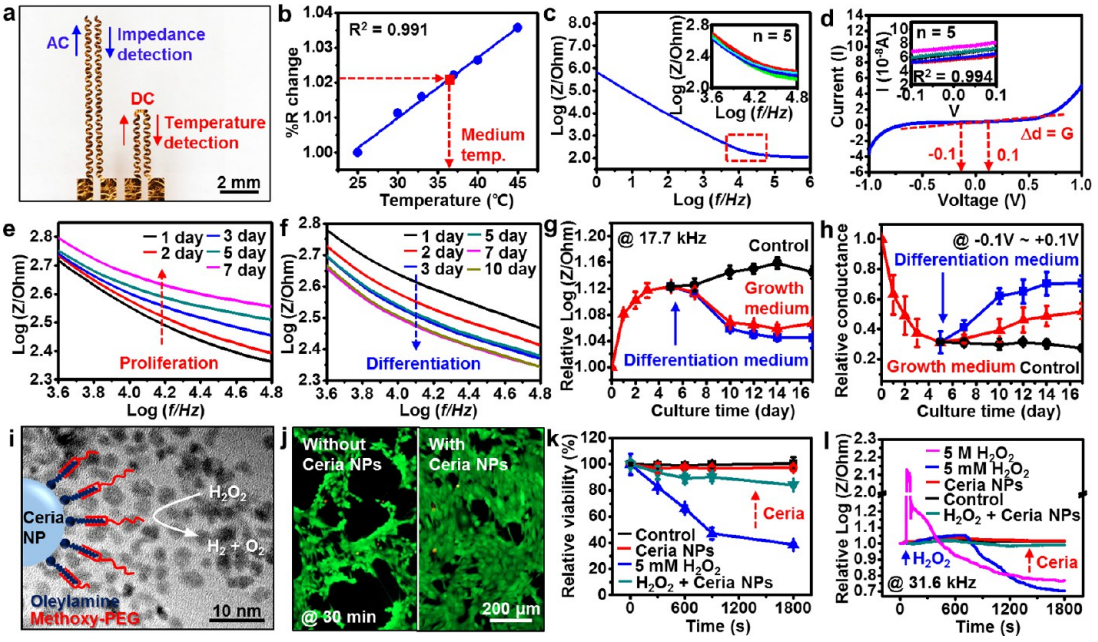

Figure 3. Physiological monitoring of C2C12 myoblasts by impedance/temperature sensors and *in vitro* tests of the efficacy of ROS scavenging nanoparticles. (a) Impedance and temperature sensors integrated on a PDMS substrate. (b) Calibration curve of temperature sensor: normalized resistance (% *R* change) as a function of temperature. The red arrow indicates the temperature of the growth medium during the culture. (c) Electrical characterization of the impedance sensor in the growth medium at 37 °C. Impedance curve measured from 1 Hz to 1 MHz with a bias voltage of 0.01 V. The inset shows the magnified view of the red-dotted region. Repeated measurements show minor deviations. (d) Current−voltage (*I*−*V*) curve, whose slope indicates the conductance. The inset shows the magnified view. Repeated measurements confirm the stability of the sensor. (e, f) The impedance curve changed as (e) the proliferation and (f) the differentiation proceeded. (g) Impedance value measured at 17.7 kHz as the culture proceeded. Red and blue curves show the cells in growth and differentiation media, respectively. The control (black) used human dermal fibroblasts. (h) Conductance values calculated from *I*−*V* curves with a range from −0.1 to +0.1 V. (i) Schematic illustration and TEM image (background image) of ROS-scavenging ceria nanoparticles. The ceria nanoparticles (Ceria NPs) are functionalized by oleylamine and methoxy-PEG. (j, k) Fluorescence image of C2C12 myoblasts (stained with calcein AM) after 30 min of H_2O_2/Ceria NP treatment (j) and relative viability plot from fluorescence images (k). (l) Plots of impedance as a function of time in different treatment groups.

The detailed characterization setups are described in Figure S5 in the Supporting Information. Figure 3e,f show changes in impedance during the proliferation and differentiation of C2C12 myoblasts, respectively (Figure S6b,d in the Supporting Information). The cells on electrodes act as insulating barriers[35] that impede the contact between electrodes and conductive media, thereby increasing the measured impedance while decreasing the measured conductance as cells proliferate (Figure 3e and Figure S6a−c in the Supporting Information). Formation of myotubes during myogenic differentiation increases conductance and thereby reduces impedance (Figure 3f and Figure S6d,e in the Supporting Information).[36] Figure 3g shows time-dependent impedance changes at 17.7 kHz with respect to cell physiology changes. Fibroblasts that do not form conducting tubular structures[36] are used as a control. Such comparison illustrates that proliferation increases impedance, while differentiation (in growth medium or differentiation medium) decreases impedance. The corresponding conductance measurements exhibit opposite trends (Figure 3h).

Testing Novel Nanomaterials on a Muscle-on-a-Chip *in Vitro*. Testing novel biomolecules or pharmaceutical materials without sacrificing animals is an important goal that many researchers have been pursuing.[27−29] The cell-culture substrate equipped with electronic sensors can provide quantitative information about changes in cellular condition within a short period of time that cannot be obtained by a microscope. As a demonstration, we design a skeletal muscle ischemia model using C2C12 myoblasts. The C2C12 myoblasts cultured on the cell-culture platform for a concept of muscle-on-a-chip were aligned for mimicking *in vivo* native condition. Ischemia-induced reactive oxygen species (ROS) decrease cell viability and cause inflammation;[37] therefore, scavenging ROS is important. Several nanomaterials and molecules have been proposed to suppress ROS generation.[38] Ceria nanoparticles are an attractive candidate for this purpose (Figure 3i)[39] and prepared as described in Figure S7 in the Supporting Information. The relevant concentrations of hydrogen peroxide (H_2O_2) and ceria nanoparticles are optimized as shown in Figure S8a−c in the Supporting Information. Then, C2C12 myoblasts are exposed to 5 mM H_2O_2 to simulate ischemia-induced ROS, and fluorescence images (Figure 3j and Figure S8d in the Supporting Information) are obtained. The use of ceria nanoparticles improves cell viability, and quantitative comparison of living cells (Figure 3k) confirms the effects of

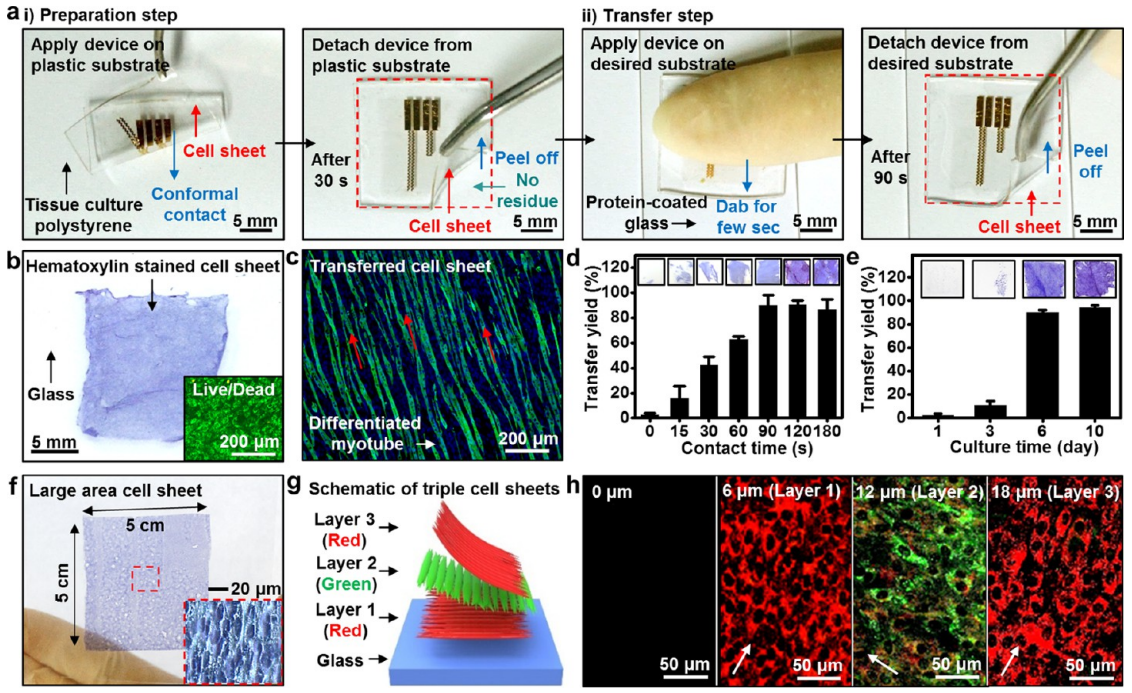

Figure 4. Transfer printing of C2C12 cell sheets. (a) Images of the cell sheet transfer printing process. (b) Image of the transferred cell sheet stained with hematoxylin on the protein-coated glass substrate. The inset shows its live/dead viability assay image, stained with calcein AM (green) and ethidium homodimer-1 (red). (c) The myosin heavy chains are maintained after the cell sheet transfer. The red arrows indicate the aligned orientation. (d, e) Plot of the transfer yields of cell sheets as a function of contact time in the transfer step (d) or as a function of culture time (e). The insets show images of transferred cell sheets. (f) Image of a 5 × 5 cm region of a hematoxylin-stained cell sheet and its magnified view (inset). (g) Schematic diagram of three cell sheets transferred layer by layer with orthogonal orientations. (h) Confocal images of the three-layered cell sheets. Images are captured at a depth interval of 6 μm. The white arrows indicate the direction of cell alignments.

ceria nanoparticles on ROS scavenging. This cell viability, represented by the impedance change, can be monitored by the instrumented cell-culture platform (Figure 3l). Treatment with 5 M H_2O_2 in differentiated C2C12 cells causes instant death in the majority of cells, resulting in a sudden, dramatic increase in impedance. Then impedance slowly decreases over 30 min as dead cells gradually detach from the substrate and conductive media flows between dead cells and electrodes. Treatment with 5 mM H_2O_2 induces similar but slower changes in impedance. However, treatment with 5 mM H_2O_2 in the presence of ceria nanoparticles yields only minimal changes in impedance.

Transfer Printing Cultured Cell Sheets *in Vitro*. Cell sheets cultured and differentiated on our soft instrumented cell-culture platform can be applied to *in vivo* therapies *via* scaffold-free localized treatments. Through continuous monitoring of cells during the preparation of cell sheets, the cell condition and degree of differentiation can be confirmed before applying the cell sheets to biological systems, which can be carried out using transfer printing.[40] The transfer printing process of the cell sheet from the cell-culture platform to the receiving substrate (protein-coated glass) is shown in Figure 4a. The protein-coated glass can be assumed as the membrane of living tissue, which is composed of proteins, where the slide glass is coated with a 5 μg/cm^2 concentration of fibronectin. The complete process consists of two steps, preparation (on tissue culture polystyrene for 30 s) and transfer (on the receiving substrate for 90 s; see video 2 in the Supporting Information for details) steps. The necessity of the preparation step will be explained by the theories of fracture mechanics in Figure 5. The well-structured configuration and high viability of the transferred C2C12 cell sheet are observed by staining cells with hematoxylin and conducting viability assays (Figure 4b and inset). Differentiation characteristics are also maintained after the transfer printing (Figure 4c). Figure 4d, e present the effects of contact time during the transfer step (changes in cell-to-protein adhesion) and cell culture time (changes in cell density) on transfer yields, respectively. High transfer yields (~90%) are obtained with contact time longer than 90 s and culture time longer than 6 days. Figure 4f shows a large-area (5 cm × 5 cm) cell sheet transfer, which is critical for human applications, and Figure 4g,h provide a schematic illustration of a triple-layered cell sheet prepared using multiple transfer printings and confocal microscope images of these sheets, respectively (video 3 in the Supporting Information).

Theoretical Analysis of Cell Sheet Transfer Printing Mechanics. Figure 5 shows a highly simplified theoretical explanation for the newly invented cell sheet transfer printing process. In view of fracture mechanics, the crack propagation criterion on an interface is $G = \Gamma$,

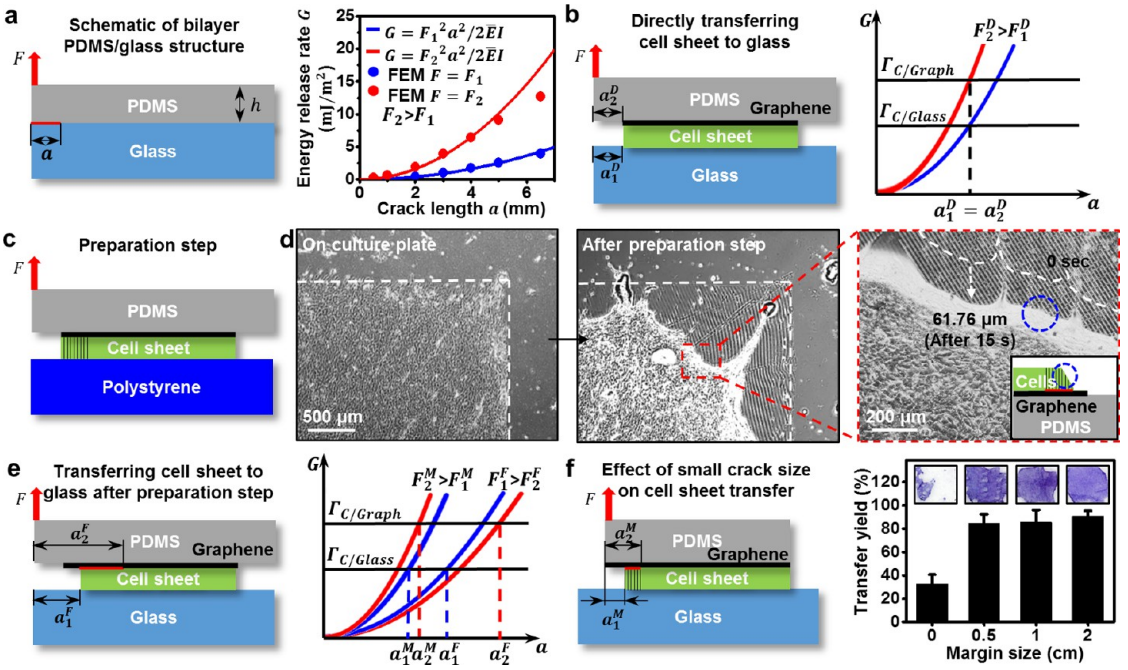

Figure 5. Fracture mechanics explanation of cell sheet transfer printing. (a) Analytical (curve) and FEM (dot) results of the energy release rate *G versus* crack length *a* under two different peeling forces. (b) When directly transferring a cell sheet onto protein-coated glass without the preparation step, the critical force to propagate a crack along the cell−glass interface (F_1^D) is lower than that along the cell−graphene interface (F_2^D), suggesting that the cell sheet cannot be transferred to glass. (c) During the preparation step, the edge of the cell sheet is damaged due to stress concentration at the crack tip while peeling the PDMS layer. (d) The damage at the edge of the cell sheet is visible under phase-contrast microscopy after the preparation step. (e) During the final transfer step, a relatively long cell−graphene interface defect introduced during the preparation step drops the critical force to propagate a crack along this interface (F_2^F) lower than that along the cell−glass interface (F_1^F); hence the cell sheet can be successfully transferred. (f) If there is no PDMS margin, *i.e.*, the whole PDMS surface is covered by graphene, the cell−graphene interface defect zone is much smaller, and hence the force to propagate a crack along the cell−graphene interface (F_2^M) is not lowered enough to facilitate successful transfer.

where G is the energy release rate (that is, the strain energy dissipated when the cracked interface advanced a unit area) and Γ is the interface toughness, which is an intrinsic interface property. As both graphene and cell sheets are much thinner than the PDMS substrate, they both can be overlooked when computing G because they store negligible strain energy. Therefore, like the other transfer printing models,[41] we simplify the cell sheet transfer printing problem to a 2D plane strain model of PDMS on glass, as illustrated by the schematic in Figure 5a, with PDMS thickness h, interfacial crack size a, and vertical peel force F. The interfacial crack size a represents the area of PDMS without graphene or cell coverage, which will also be referred to as the margin size later. As glass is 6 orders of magnitude stiffer than PDMS, we can model the glass as a rigid substrate. By also assuming the total length of the PDMS layer is much longer than a, analytical derivation of the energy release rate (Figure S9 in the Supporting Information) gives

$$G = \frac{F^2 a^2}{2\bar{E}I} \tag{1}$$

where $\bar{E}I$ is the plane strain bending rigidity of the PDMS layer. Equation 1 and finite element modeling (FEM) results (section 1.1 in the Supporting Information) of the $G(F, a)$ relation are plotted in the graph of Figure 5a. Both results indicate that G increases monotonically with both a and F. The following qualitative explanation will be based on this simple fact.

Figure 5b explains why the cell sheet cannot be directly transferred to protein-coated glass. Although graphene and the cell sheet are too thin to be considered in fracture mechanics models, they are intentionally made visible in the schematic for illustration. We label the initial crack size on the PDMS−glass interface up to cell−glass adhesion as a_1^D, where "D" represents the "direct transfer" step and "1" denotes the cell−glass interface, and up to the cell−graphene interface as a_2^D, where "2" denotes the cell−graphene interface. In the direct transfer step, $a_1^D = a_2^D$ is assumed. As $\Gamma_{c/graph} > \Gamma_{c/glass}$,[23,42] there will be one intersection defined by $a = a_1^D$ and $G = \Gamma_{c/glass}$, which is lower than the other intersection defined by $a = a_2^D$ and $G = \Gamma_{c/graph}$, as shown in the graph of Figure 5b. When $G = \Gamma$ and a is given, F_1^D and F_2^D can be calculated using eq 1. The two F's obtained in this way will make the $G-a$ curves pass through the two intersections, respectively. Because of the monotonic relation between G and F as given by eq 1, it is determined that the peel force needed to delaminate the cell−glass interface (F_1^D) is smaller than that for the cell−graphene

interface (F_2^D), suggesting that the cell sheet is easier to delaminate along the cell−glass interface and therefore cannot be transferred to the glass substrate successfully.

The outcome will be different if the preparation step shown in Figure 5c is taken before transferring the cell sheet to protein-coated glass. As cell attachment on glass, polystyrene, and PDMS is reported to be very similar[43] and cell−graphene adhesion is much higher than cell−PDMS (Figure 2a) or cell−glass adhesion,[23,42] it is reasonable for us to assume $\Gamma_{c/graph} > \Gamma_{c/polystyrene}$. Therefore, the cell sheet will not be transferred onto polystyrene during the preparation step for the same reason as explained in Figure 5b. However, edge damage can be found in the cell sheet after the preparation step, as evidenced by the phase-contrast microscope images in Figure 5d (also see video 4 in the Supporting Information). It has been reported that muscle cells react to mechanical stretches by contraction,[44] which is presumed to lead to significant shear-induced interfacial delamination between the cell sheet and graphene during peeling off, as highlighted by the red line in the inset of Figure 5d. When the cell sheet is put into contact with the protein-coated glass immediately after the preparation step, the adhesion between the cell sheet and protein-coated glass is assumed to be complete. Hence, as illustrated by Figure 5e, the initial crack lengths for the final transfer step become a_1^F and a_2^F, and a_2^F is larger than a_1^F. When a_2^F is large enough, $F_2^F < F_1^F$ can be reached following the same procedure as that used to reach the conclusion of $F_1^D < F_2^D$ in Figure 5b, indicating that the cell−graphene interface will delaminate at a smaller peel force. Therefore, the cell sheet can be successfully transferred onto protein-coated glass after the preparation step is performed.

When there is no PDMS margins, *i.e.*, when the PDMS surface is fully covered by graphene, the edge damage of cells is less significant during the preparation step due to smaller stress singularity (Figure S10 in the Supporting Information), and hence, a_2^M will be only slightly larger than a_1^M (where "M" denotes margin effect), as shown in Figure 5f (also see section 1.2 in the Supporting Information). According to the graph in Figure 5e, $F_1^M < F_2^M$, and hence, the cell−glass interface will first delaminate and the transfer will fail. This hypothesis is validated by the experimental results shown in the right panel of Figure 5f, and it explains why maintaining reasonable PDMS margin size is critical for the success of cell sheet transfer. Explanations for other effects that govern the success of transfer printing such as moisture and cell sheet continuity are offered in Figures S11 and S12 in the Supporting Information (also see sections 1.3 and 1.4 in the Supporting Information).

***In Vivo* Cell Sheet Transfer Printing for Cell Sheet Therapy.** To investigate the therapeutic effects of *in vivo* cell sheet transfer printing on scarred muscles in mice, we use green fluorescent protein (GFP)-transfected C2C12 myoblasts and observe modalities to evaluate tissue organization. We graft aligned and differentiated monolayer or five-layered C2C12 cell sheets onto the scarred area on the hindlimbs of mice (Figure 6a; surgical procedure is described in Figure S13 in the Supporting Information). The temperature changes during the cell sheet transfer printing are measured by the temperature sensor of the instrumented cell-culture platform (Figure S14a,b in the Supporting Information). Fast transfer printing (∼90 s) causes minimal body temperature changes (∼1.5 °C).

Transplanted cell sheets are labeled with a cell tracer (DiD) and monitored over time by measuring the fluorescence. Fluorescence is detected on the scarred area, even after 7 days, while no signal is observed in the opposite hindlimb sites (see fluorescence data of five-layered cell sheet in Figure 6b and of both monolayer and five-layer in Figure S15a in the Supporting Information). Fluorescence microscope images of sectioned tissue slices from transferred sites show the growth of the transplanted five-layered cell sheets 7 days after transfer printing (Figure 6c), which is consistent with *in vivo* fluorescence imaging results. The capability to maintain the organization and function of a transplanted cell sheet can maximize the therapeutic effect of localized cell therapy at the wound site.

Microcomputed tomography (micro-CT) also confirms the growth of muscular tissues in the transplanted region (Figure 6d). The white arrows indicate the operation site. Comparison between the first and second frame of Figure 6d highlights removed muscle tissues. Importantly, 7 days after transplantation of the cell sheet, muscle tissues are regenerated (Figure 6d third frame), while no recovery is observed without cell sheet transfer after the surgery (Figure 6d fourth frame; the inset shows the preoperation image of the negative experiment group). Hematoxylin and eosin staining images reveal that five-layered cell sheets have grown at transferred sites (Figure 6e). On the other hand, atrophic changes in muscles occur in the scarred muscles without cell sheet transplantation (Figure 6f). The monolayer cell sheet also shows therapeutic effects on the scarred region (Figure S15b in the Supporting Information). The abundant proliferation and differentiation of C2C12 myoblasts in five-layered cell sheets transferred into scarred muscle sites are observed through the detection of GFP expression, as shown in Figure 6g,h (monolayer cell sheet data are also shown in Figure S15c in the Supporting Information). Vascularization is also observed by CD31 staining (Figure 6i).

DISCUSSION

Multifunctional cell-culture platforms provide not only their originally dedicated function (*e.g.*, acting as a scaffold for tissue engineering) but also novel functions, such as real-time physiological monitoring of proliferation and differentiation, aligning cultured

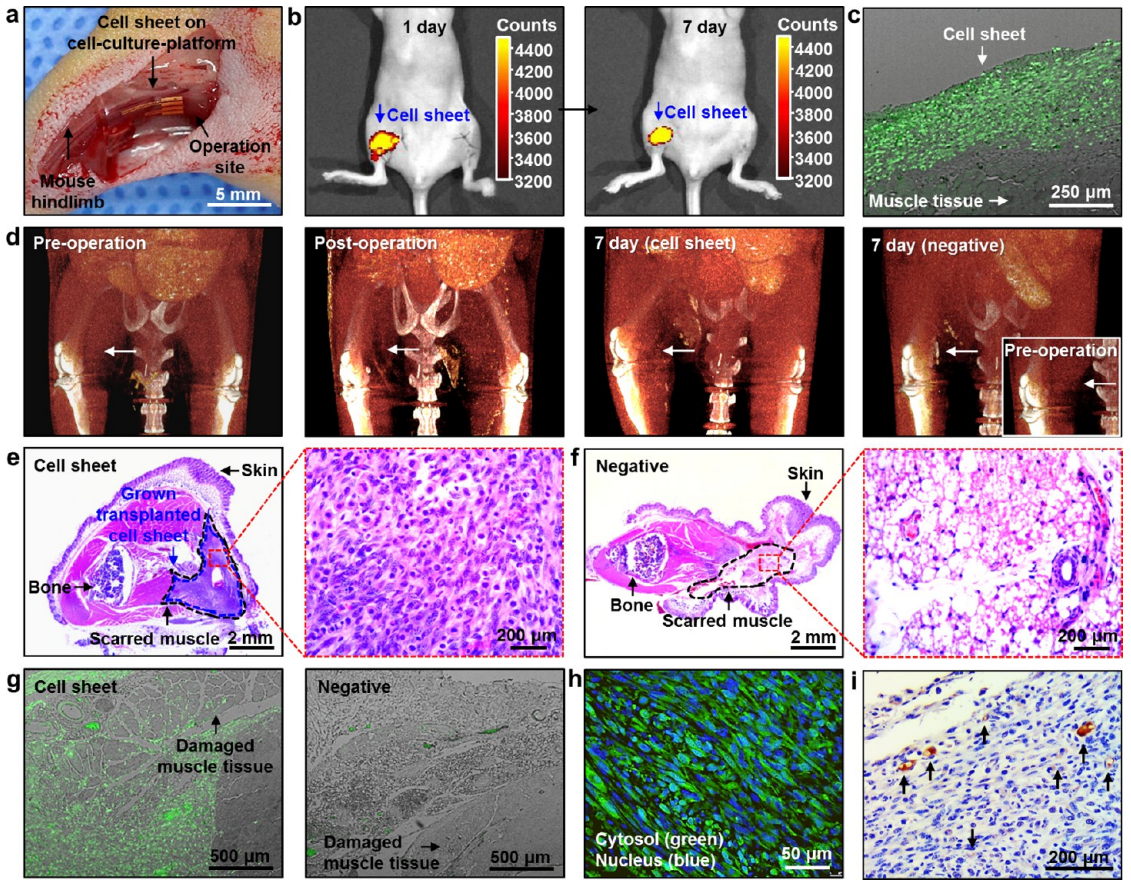

Figure 6. Investigation of therapeutic effects of the cell sheet transplantation in scarred mouse muscles. (a) Image of cell sheet transfer printing applied to scarred hindlimb muscle in a mouse. (b) *In vivo* fluorescence imaging at 1 day (left) and 7 days (right) after transfer printing of the five-layered C2C12 cell sheets labeled with cell tracers (DiD). (c) Proliferation of transfer-printed cells (GFP-expressing C2C12 myoblasts) at the operation site 7 days after transplantation. (d) CT images of the operated mice: (from left to right) preoperation, postoperation, 7 days after cell sheet transplantation (five-layered), and negative control (no cell sheet transplantation). The white arrows indicate the operation site. The inset shows the preoperation image of the negative experiment group. (e, f) Hematoxylin and eosin staining of the operated hindlimb 7 days after transplantation of the cell sheet (five-layered) and without the cell sheet transplantation (negative control) for morphological observations. The red-dotted boxes show magnified views. (g) Proliferation of the cell sheet around the damaged muscles, as shown by expression of GFP. (h) Differentiation of the cell sheet around the damaged muscles. (i) Vascularization (black arrows) in the region of transferred cell sheets 7 days after transplantation.

cells, testing new nanomaterials and chemicals *in vitro*, and transfer printing cell sheets to *in vivo* systems for localized cell therapy. We have achieved these novel functions in our current study by the monolithic integration of functional nanomaterials and ultrathin electronics to elastomeric substrates as well as by the effective utilization of key design features and fabrication techniques of stretchable electronics.

The soft instrumented cell-culture platform developed in this study is also applicable in regenerative medicine, the ultimate goal of tissue engineering scaffolds, by our established unique system and protocol for transfer printing of cell sheets. Generally, thermoresponsive materials (such as PIPAAm-grafted culture plate[13−15] or Tetronic-tyramine hydrogel[45,46]) have been widely used for transferring cell sheets. These previous transfer processes require low temperatures and long times (20 °C for 30 min of PIPAAm; 4 °C for 10 min of Tetronic-tyramine hydrogel). However, the current method shortens the required time (<3 min) without temperature changes, resulting in safe and fast transfer printings. Thereby, aligned and differentiated C2C12 cell sheets cultured on the soft instrumented cell-culture platform are successfully transfer-printed to desired locations, such as scarred muscles of animal models. The low system modulus of our cell-culture platform is matched with the modulus of target tissues, which maximizes transfer printing yields and thus enables easy and successful implantation of multiple cell sheets onto localized, diseased regions. *In vivo* muscular tissue regeneration was observed and characterized by multiple imaging methodologies. The spatial confinement of transplanted cell sheets near wounded regions enhances therapeutic effects and the efficiency of the cell therapy. The localization of cells with high density (*e.g.*, multiple, stacked cell sheets) is advantageous in comparison with other cell deployment methods, such as needle injection.[46]

Furthermore, transfer printing of fully differentiated cell sheets may promote therapeutic effects, as the previous study[47] has reported that transplantation of highly differentiated muscle cells enhances muscle regeneration. Meanwhile, insufficient vascular supply hampers the long-term therapy of three-dimensional cell sheet transplantation.[48] Several studies have reported that the secretion of angiogenic growth factors, *i.e.*, vascular endothelial growth factors (VEGFs), by the muscle tissues in necrotic conditions induces the enhancement of angiogenesis.[49] The observation of newly formed vessels within the transfer-printed cell sheets indicates the success of the muscle regeneration.[50]

Our cell sheet transfer printing strategy can be further applied onto a variety of types of cells. In regenerative medicine, human mesenchymal stem cells (hMSCs) have been actively studied to target multiple diseased organs, especially the heart[15] and brain.[51] In this study, our soft instrumented cell-culture platform provides good adhesion and proliferation properties to hMSCs as well as a platform to transfer-print hMSC cell sheets onto various desired substrates successfully while retaining the original structures (Figure S16a,b in the Supporting Information). In addition, our transfer printing strategy enables the *in vivo* transfer printing therapy of hMSC cell sheets onto murine brain and heart tissues as shown in an IVIS study (Figure S16c,d in the Supporting Information).

CONCLUSION

Our instrumented soft cell-culture platform provides not only its originally dedicated function of an ECM for tissue engineering but also novel functions, such as aligning plated cells, monitoring physiological cues, testing new nanomaterials *in vitro*, and transfer printing cell sheets to *in vivo* systems. In our study, graphene nanoribbons had enhanced cell adhesion, promoted differentiation, and led to anisotropic arrangement of C2C12 myoblasts, mimicking the native muscle tissue. Additionally, the characteristics of cultured cells could be monitored by integrated sensors (impedance, conductance, and temperature). We have also used the muscle-on-a-chip platform to ascertain the effects of ceria nanoparticles on ROS scavenging. By engineering the interface between the current platform and the cell sheet through a preparation step, we have successfully developed a safe, simple, and highly efficient protocol for *in vitro* and *in vivo* cell sheet transfer printing. The theoretical analysis enlightens the underlying mechanics and physics of the transfer printing protocol, which can provide fundamental insights on the potentially simplified transfer printing of cell sheets for broader users, such as clinicians. In summary, the soft instrumented cell-culture platform delivers innovative multipurpose cell-culture systems and contributes to the research and development of tissue engineering. It broadens the range of *in vitro* applications, such as deliberate cell regulations, *in situ* and real-time physiological monitoring, and simple yet precise drug screening, as well as enables clinically effective *in vivo* therapeutic applications. Further work will focus on new applications of the current platform to other disease models.

METHODS

Fabrication of the Soft Instrumented Cell-Culture Platform. Graphene was synthesized using the chemical vapor deposition growth process[52] and was grown on copper foil (Alfa Aesar) at 1000 °C with a mixture of methane (20 sccm, 1.6 Torr) and hydrogen (8.4 sccm, 0.8 Torr). The fabrication process of the current cell-culture platform (schematic illustration) and the AutoCAD design of the sensors are provided in Figure S1a,b in the Supporting Information, respectively. Ni was deposited onto a Si wafer (test grade, 4Scinece) by thermal evaporation. Next, 7 nm of Cr and 150 nm of Au were deposited onto Ni-deposited Si wafers by thermal evaporation and patterned by photolithography and wet etching. Then, the graphene was transferred onto the sample and patterned with 5 μm lines and 5 μm spaces with photolithography and reactive ion etching using O_2 plasma (O_2 flow rate of 100 sccm, chamber pressure of 100 mTorr, 150 W RF power for 25 s). The sample was spin coated with poly(methyl methacrylate) (PMMA; A4, Microchem; ~300 nm) at 3000 rpm for 30 s and was then immersed in Ni etchant for 30 min. The sample was transferred onto low-modulus PDMS (Sylgard 527, Dow Corning; part A to B in a ratio of 1:2; thickness of 600 μm) and dried in an oven at 70 °C for 10 min. Finally, the PMMA was removed with acetone. The elastic modulus of the sample was measured with a digital force meter (Mark-10). Electrical measurements by impedance and temperature sensors were carried out with an electrochemical workstation (CHI660E, CH Instrument) and a parameter analyzer (B1500A, Agilent), respectively, which were connected with anisotropic conductive films.[11]

Measurement of the Protein Interaction Force of Graphene. All data describing the adhesion forces between fibronectin molecules and graphene were obtained by an atomic force microscope (Dimension Icon, Bruker). For functionalization of the AFM tip with fibronectin, the tip was cleaned with a UV/ozone cleaner (Yuil Ultra Violet System) for 3 min, following by additional cleaning with acetone. Next, the tip was soaked in fibronectin solution (5 μg/mL in distilled water; Invitrogen) and completely dried at room temperature. Spring constants of cantilevers (ScanAsyst-Air, Bruker probes) were calibrated using the thermal tune function, and all AFM experiments were conducted in PeakForce QNM mode.

Cell Culture. C2C12 myoblasts (CRL-1772; ATCC), human dermal fibroblasts (PCS-201-012; ATCC), and human mesenchymal stem cells (PT-2501; Lonza) were used for experiments. C2C12 myoblasts were cultured in two types of media: proliferation medium, composed of Dulbecco's modified Eagle's medium (DMEM) supplemented with 10% fetal bovine serum (FBS, Gibco) and 1% penicillin–streptomycin (PS, Gibco), and differentiation medium (to induce myotube formation) composed of DMEM supplemented with 5% horse serum (Gibco) and 1% PS. Human dermal fibroblasts were cultured in DMEM supplemented with 10% FBS and 1% PS. Human mesenchymal stem cells were cultured in MSCGM mesenchymal stem cell growth medium (Lonza). The cells were cultured under the standard culture conditions of 37 °C and 5% CO_2. The cells were seeded onto the cell-culture platform at different densities according to each experiment: 2×10^4 cells/cm^2 for observation

of cellular behaviors on the patterned graphene nanoribbons (Figure 2) and measuring electrical signals of cells (Figure 3e−h) or 5×10^4 cells/cm^2 to demonstrate the muscle-on-a-chip (Figure 3i−l) and transfer printing of cell sheets (Figures 4 and 6; note, cells were plated at 2×10^4 cells/cm^2 for Figure 4e).

Cellular Characteristics on Patterned Graphene. To observe the effects of the patterned graphene on cellular behaviors, the cells were stained with a live/dead viability kit (Life Technologies) using 0.5 μM calcein AM and 5 μM ethidium homodimer-1 in growth medium and were observed using a fluorescence microscope (Eclipse Ti, Nikon). The C2C12 cell alignment on the patterned graphene was monitored by the differential interference contrast (DIC) mode using a confocal microscope (TCS SP8 STDE, Leica). DIC images of cell alignment were captured every 15 min for 48 h while incubating in the standard culture conditions. To observe the alignment of cytoskeletal actin, the cells were counterstained with rhodamine phalloidine (Life Technologies). The cultured cells were fixed in 4% paraformaldehyde solution (Sigma-Aldrich) diluted in phosphate-buffered saline (PBS) for 10 min and permeabilized in cytoskeleton (CSK) buffer (150 mM sucrose, 50 mM NaCl, 3 mM $MgCl_2$, 50 mM Trizma-base, and 0.5% Triton X-100, pH 6.8) for 5 min. Next, the cells were incubated in block buffer (10% FBS and 0.1% Tween-20 in PBS) for 2 h to block nonspecific binding sites and were subsequently incubated with paxillin (1:100; Invitrogen) for 1 h at 37 °C. After washing, the samples were counterstained with DAPI and observed under a fluorescence microscope (Eclipse Ti, Nikon). To observe myotube formation, the cultured cells were fixed in 4% paraformaldehyde solution, permeabilized in CSK buffer, and blocked in blocking buffer. The cells were then incubated with antimyosin heavy-chain antibodies (1:100 dilution; Abcam), followed by incubation with Alexa Fluor 488 donkey anti-mouse IgG (1:100 dilution; Abcam) for 1 h at 37 °C. After washing, the cells were counterstained with DAPI and observed under a fluorescence microscope (Eclipse Ti, Nikon).

Preparation of Ceria Nanoparticles. To synthesize ceria nanoparticles, 1 mM (0.4 g) cerium(III) acetate (98%, Sigma-Aldrich) and 12 mM (3.2 g) oleylamine (approximate C18 content of 80−90%, AcrosOrganics) were added to 15 mL of xylene (98.5%, Sigma-Aldrich). The mixed solution was sonicated for 15 min at room temperature and then heated to 90 °C. One milliliter of distilled water was injected into the solution under vigorous stirring at 90 °C, and the solution color changed to an off-white color, indicating that the reaction had occurred. The resulting mixture was aged for 3 h at 90 °C to give a light yellow colloidal solution, which was then cooled to room temperature. Acetone (100 mL) was added to the precipitated ceria nanoparticles. The precipitate was washed with acetone using centrifugation, and the resulting ceria nanoparticles were easily dispersible in organic solvents, *e.g.*, chloroform. For the synthesis of phospholipid-PEG-capped ceria nanoparticles, the ceria nanoparticles dispersed in chloroform were encapsulated by a PEG-phospholipid shell. First, 3 mL of ceria nanoparticles in $CHCl_3$ (10 mg/mL) was mixed with 3 mL of $CHCl_3$ solution containing 30 mg of mPEG-2000 PE. The solvent was then evaporated using a rotary evaporator and incubated at 70 °C in a vacuum for 1 h to completely remove the chloroform. The addition of 5 mL of distilled water yielded a clear and light yellowish suspension. After filtration, excess mPEG-2000 PE was removed using ultracentrifugation. Purified phospholipid-PEG-capped ceria nanoparticles were dispersed in distilled water.

Multilayered Cell Sheet. Three samples of cell sheets were prepared on the cell-culture platform, where each cell sheet was previously stained with fluorescence dye, colored with DiD (red; two samples; Invitrogen) or DiO (green; one sample; Invitrogen). Each cell sheet was transferred in the order of red, green, red, and sheets were stacked on top of each other. The arrangement of multilayered cell sheets was observed using a confocal microscope (TCS SP8 STDE, Leica). To clearly visualize each cell sheet, the color intensities of the captured images were modified using the Leica Application Suite (Leica).

Mouse Scarred Muscle Model. All experiments on animals were approved by the animal care committee at Seoul National University Hospital. Six-week-old male BALB/c nude mice were anesthetized by intraperitoneal injection with a mixture of zolazepam and xylazine. A surgical skin incision (1.5 cm) was made in the ventral aspect of the right thigh beginning near the groin. Subsequently, the medial thigh muscle was dissected 5 mm proximal to and along the course of the deep femoral branch. The dissection continued laterally 5 mm from and along the bundle of the femoral nerve, artery, and vein. The entire medial thigh muscle was excised.

Micro-CT. After the cell sheet transplantation (1 layer, 5 layers, or none; each group $N = 4$) to the scarred muscles in the hindlimb, the therapeutic effect was monitored over time by micro-CT. The micro-CT was performed using a cone-beam-type commercial preclinical CT scanner (NFR-Polaris-G90C, NanoFocusRay) with the following imaging parameters: tube voltage, 50 kVp; tube current, 100 μA; field of view, 35 mm $\times$ 35 mm; matrix, 512 $\times$ 512; slice thickness, 0.054 mm. Three-dimensional reconstructed images were obtained using OsiriX (version 4.0, 32 bit, OsiriX Foundation).

***In Vivo* Fluorescent Imaging.** For fluorescent imaging, Balb/c nude mice (female, ages 6−8 weeks) were subjected to operation with cell tracer (DiD)-labeled GFP-expressing cell sheets and anesthetized by intraperitoneal injection. Imaging of mice was carried out with an IVIS Spectrum instrument (IVIS, PerkinElmer) in epifluorescence mode equipped with 644 and 665 nm filters for excitation and emission, respectively, from 1 day after transplantation. Measurements of the fluorescence signal from each cell sheet were made using Living Image Software 4.0 (PerkinElmer).

Histology. All tissues were embedded in paraffin and sectioned to 4 μm thickness. Histology samples for morphology visualization were stained by hematoxylin and eosin using standard protocols. For immunofluorescence staining, the prepared paraffin sections were dewaxed, hydrated, and treated with 0.01% protease XXIV (Sigma-Aldrich) in PBS for 20 min at 37 °C. The specimens were then stained with primary anti-GFP antibodies (Santa Cruz Biotechnology) according to the manufacturer's instructions. Protein expression was visualized with Alexa Fluor 488-conjugated secondary antibodies (Invitrogen). All images were acquired using an inverted fluorescence microscope (DM5500 B, Leica). In order to detect vascularization in organized tissues from the cell sheet, immunohistochemistry was performed using the following steps with anti-CD31 antibodies (Novus Biologicals). First, endogenous peroxidase and protein were blocked with a solution of 0.3% H_2O_2 and goat serum (Dako) to prevent nonspecific antibody binding. After 30 min, the tissues were then incubated with the primary anti-CD31 antibody for 1 h, washed, and incubated with horseradish peroxidase-conjugated goat anti-rabbit secondary antibodies (Santa Cruz Biotechnology) for 1 h. After additional washes, vascularization was evaluated by staining with 3,3′-diaminobenzidine peroxidase substrate (Dako).

Conflict of Interest: The authors declare no competing financial interest.

Acknowledgment. This work was supported by IBS-R006-D1. This work was also supported by a grant from the Basic Science Research Program of the National Research Foundation of Korea (NRF), funded by the Ministry of Science, ICT, and Future Planning (2012R1A1A1004925). This work was supported by the Seoul National University Research Grant. N.L. acknowledges the U.S. NSF CMMI award under Grant No. 1301335.

Supporting Information Available: Additional text, table, 16 figures, and 4 videos. This material is available free of charge *via* the Internet at http://pubs.acs.org.

REFERENCES AND NOTES

1. Levenberg, S.; Huang, N. F.; Lavik, E.; Rogers, A. B.; Itskovitz-Eldor, J.; Langer, R. Differentiation of Human Embryonic Stem Cells on Three-Dimensional Polymer Scaffolds. *Proc. Natl. Acad. Sci. U.S.A.* **2003**, *100*, 12741–12746.
2. Dvir, T.; Timko, B. P.; Kohane, D. S.; Langer, R. Nanotechnological Strategies for Engineering Complex Tissues. *Nat. Nanotechnol.* **2011**, *6*, 13–22.

3. Sun, J. Y.; Zhao, X.; Illeperuma, W. R.; Chaudhuri, O.; Oh, K. H.; Mooney, D. J.; Vlassak, J. J.; Suo, Z. Highly Stretchable and Tough Hydrogels. *Nature* **2012**, *489*, 133–136.
4. Tian, B.; Liu, J.; Dvir, T.; Jin, L.; Tsui, J. H.; Qing, Q.; Suo, Z.; Langer, R.; Kohane, D. S.; Lieber, C. M. Macroporous Nanowire Nanoelectronic Scaffolds for Synthetic Tissues. *Nat. Mater.* **2012**, *11*, 986–994.
5. Straub, B.; Meyer, E.; Fromherz, P. Recombinant Maxi-K Channels on Transistor, A Prototype of Iono-Electronic Interfacing. *Nat. Biotechnol.* **2001**, *19*, 121–124.
6. Sekitani, T.; Zschieschang, U.; Klauk, H.; Someya, T. Flexible Organic Transistors and Circuits with Extreme Bending Stability. *Nat. Mater.* **2010**, *9*, 1015–1022.
7. Viventi, J.; Kim, D. H.; Vigeland, L.; Frechette, E. S.; Blanco, J. A.; Kim, Y. S.; Avrin, A. E.; Tiruvadi, V. R.; Hwang, S. W.; Vanleer, A. C.; *et al*. Flexible, Foldable, Actively Multiplexed, High-Density Electrode Array for Mapping Brain Activity *in Vivo*. *Nat. Neurosci.* **2011**, *14*, 1599–1605.
8. Sekitani, T.; Noguchi, Y.; Hata, K.; Fukushima, T.; Aida, T.; Someya, T. A Rubberlike Stretchable Active Matrix Using Elastic Conductors. *Science* **2008**, *321*, 1468–1472.
9. Kim, D. H.; Lu, N.; Ma, R.; Kim, Y. S.; Kim, R. H.; Wang, S.; Wu, J.; Won, S. M.; Tao, H.; Islam, A.; *et al*. Epidermal Electronics. *Science* **2011**, *333*, 838–843.
10. Keplinger, C.; Sun, J. Y.; Foo, C. C.; Rothemund, P.; Whitesides, G. M.; Suo, Z. Stretchable, Transparent, Ionic Conductors. *Science* **2013**, *341*, 984–987.
11. Son, D.; Lee, J.; Qiao, S.; Ghaffari, R.; Kim, J.; Lee, J. E.; Song, C.; Kim, S. J.; Lee, D. J.; Jun, S. W.; *et al*. Multifunctional Wearable Devices for Diagnosis and Therapy of Movement Disorders. *Nat. Nanotechnol.* **2014**, *9*, 397–404.
12. Park, Y. J.; Lee, S. K.; Kim, M. S.; Kim, H.; Ahn, J. H. Graphene-Based Conformal Devices. *ACS Nano* **2014**, *8*, 7655–7662.
13. Nishida, K.; Yamato, M.; Hayashida, Y.; Watanabe, K.; Yamamoto, K.; Adachi, E.; Nagai, S.; Kikuchi, A.; Maeda, N.; Watanabe, H.; *et al*. Corneal Reconstruction with Tissue-Engineered Cell Sheets Composed of Autologous Oral Mucosal Epithelium. *N. Engl. J. Med.* **2004**, *351*, 1187–1196.
14. Iwata, T.; Yamato, M.; Tsuchioka, H.; Takagi, R.; Mukobata, S.; Washio, K.; Okano, T.; Ishikawa, I. Periodontal Regeneration with Multi-Layered Periodontal Ligament-Derived Cell Sheets in a Canine Model. *Biomaterials* **2009**, *30*, 2716–2723.
15. Miyahara, Y.; Nagaya, N.; Kataoka, M.; Yanagawa, B.; Tanaka, K.; Hao, H.; Ishino, K.; Ishida, H.; Shimizu, T.; Kangawa, K.; *et al*. Monolayered Mesenchymal Stem Cells Repair Scarred Myocardium after Myocardial Infarction. *Nat. Med.* **2006**, *12*, 459–465.
16. Akiyama, Y.; Kikuchi, A.; Yamato, M.; Okano, T. Ultrathin Poly(N-isopropylacrylamide) Grafted Layer on Polystyrene Surfaces for Cell Adhesion/Detachment Control. *Langmuir* **2004**, *20*, 5506–5511.
17. Engler, A. J.; Sen, S.; Sweeney, H. L.; Discher, D. E. Matrix Elasticity Directs Stem Cell Lineage Specification. *Cell* **2006**, *126*, 677–689.
18. Kim, D. H.; Song, J.; Choi, W. M.; Kim, H. S.; Kim, R. H.; Liu, Z.; Huang, Y. Y.; Hwang, K. C.; Zhang, Y.; Rogers, J. A. Materials and Noncoplanar Mesh Designs for Integrated Circuits with Linear Elastic Responses to Extreme Mechanical Deformations. *Proc. Natl. Acad. Sci. U.S.A.* **2008**, *105*, 18675–18680.
19. Bowden, N.; Brittain, S.; Evans, A. G.; Hutchinson, J. W.; Whitesides, G. M. Spontaneous Formation of Odered Structures in Thin Films of Metals Supported on an Elastomeric Polymer. *Nature* **1998**, *393*, 146–149.
20. Khang, D. Y.; Jiang, H.; Huang, Y.; Rogers, J. A. A Stretchable Form of Single-Crystal Silicon for High-Performance Electronics on Rubber Substrates. *Science* **2006**, *311*, 208–212.
21. Jiang, H.; Khang, D. Y.; Song, J.; Sun, Y.; Huang, Y.; Rogers, J. A. Finite Deformation Mechanics in Buckled Thin Films on Compliant Supports. *Proc. Natl. Acad. Sci. U.S.A.* **2007**, *104*, 15607–15612.
22. Park, S. Y.; Park, J.; Sim, S. H.; Sung, M. G.; Kim, K. S.; Hong, B. H.; Hong, S. Enhanced Differentiation of Human Neural Stem Cells into Neurons on Graphene. *Adv. Mater.* **2011**, *23*, H263–H267.
23. Hong, S. W.; Lee, J. H.; Kang, S. H.; Hwang, E. Y.; Hwang, Y. S.; Lee, M. H.; Han, D. W.; Park, J. C. Enhanced Neural Cell Adhesion and Neurite Outgrowth on Graphene-Based Biomimetic Substrates. *BioMed. Res. Int.* **2014**, *2014*, 212149.
24. Bajaj, P.; Rivera, J. A.; Marchwiany, D.; Solovyeva, V.; Bashir, R. Graphene-Based Patterning and Differentiation of C2C12 Myoblasts. *Adv. Healthcare Mater.* **2014**, *3*, 995–1000.
25. Park, J.; Park, S.; Ryu, S.; Bhang, S. H.; Kim, J.; Yoon, J. K.; Park, Y. H.; Cho, S. P.; Lee, S.; Hong, B. H.; *et al*. Graphene-Regulated Cardiomyogenic Differentiation Process of Mesenchymal Stem Cells by Enhancing the Expression of Extracellular Matrix Proteins and Cell Signaling Molecules. *Adv. Healthcare Mater.* **2014**, *3*, 176–181.
26. Kim, K. S.; Zhao, Y.; Jang, H.; Lee, S. Y.; Kim, J. M.; Kim, K. S.; Ahn, J. H.; Kim, P.; Choi, J. Y.; Hong, B. H. Large-Scale Pattern Growth of Graphene Films for Stretchable Transparent Electrodes. *Nature* **2009**, *457*, 706–710.
27. Huh, D.; Matthews, B. D.; Mammoto, A.; Montoya-Zavala, M.; Hsin, H. Y.; Ingber, D. E. Reconstituting Organ-Level Lung Functions on a Chip. *Science* **2010**, *328*, 1662–1668.
28. Huh, D.; Hamilton, G. A.; Ingber, D. E. From 3D Cell Culture to Organs-on-Chips. *Trends Cell Biol.* **2011**, *21*, 745–754.
29. Huh, D.; Leslie, D. C.; Matthews, B. D.; Fraser, J. P.; Jurek, S.; Hamilton, G. A.; Thorneloe, K. S.; McAlexander, M. A.; Ingber, D. E. A Human Disease Model of Drug Toxicity-Induced Pulmonary Edema in a Lung-on-a-Chip Microdevice. *Sci. Transl. Med.* **2012**, *4*, 159ra147.
30. Guo, J. J.; Yao, X. J.; Ning, L. L.; Wang, Q. Q.; Liu, H. X. The Adsorption Mechanism and Induced Conformational Changes of Three Typical Proteins with Different Secondary Structural Features on Graphene. *RSC Adv.* **2014**, *4*, 9953–9962.
31. Sawyer, A. A.; Hennessy, K. M.; Bellis, S. L. Regulation of Mesenchymal Stem Cell Attachment and Spreading on Hydroxyapatite by RGD Peptides and Adsorbed Serum Proteins. *Biomaterials* **2005**, *26*, 1467–1475.
32. Boontheekul, T.; Hill, E. E.; Kong, H. J.; Mooney, D. J. Regulating Myoblast Phenotype through Controlled Gel Stiffness and Degradation. *Tissue Eng.* **2007**, *13*, 1431–1442.
33. Bagnaninchi, P. O.; Drummond, N. Real-Time Label-Free Monitoring of Adipose-Derived Stem Cell Differentiation with Electric Cell-Substrate Impedance Sensing. *Proc. Natl. Acad. Sci. U.S.A.* **2011**, *108*, 6462–6467.
34. Kim, D. H.; Ghaffari, R.; Lu, N.; Wang, S.; Lee, S. P.; Keum, H.; D'Angelo, R.; Klinker, L.; Su, Y.; Lu, C.; *et al*. Electronic Sensor and Actuator Webs for Large-Area Complex Geometry Cardiac Mapping and Therapy. *Proc. Natl. Acad. Sci. U.S.A.* **2012**, *109*, 19910–19915.
35. Wegener, J.; Keese, C. R.; Giaever, I. Electric Cell-Substrate Impedance Sensing (ECIS) as a Noninvasive Means to Monitor the Kinetics of Cell Spreading to Artificial Surfaces. *Exp. Cell Res.* **2000**, *259*, 158–166.
36. Rakhilin, S.; Turner, G.; Katz, M.; Warden, R.; Irelan, J.; Abassi, Y. A.; Glass, D. J. Electrical Impedance as a Novel Biomarker of Myotube Atrophy and Hypertrophy. *J. Biomol. Screen.* **2011**, *16*, 565–574.
37. Eltzschig, H. K.; Eckle, T. Ischemia and Reperfusion--from Mechanism to Translation. *Nat. Med.* **2011**, *17*, 1391–1401.
38. Karakoti, A.; Singh, S.; Dowding, J. M.; Seal, S.; Self, W. T. Redox-Active Radical Scavenging Nanomaterials. *Chem. Soc. Rev.* **2010**, *39*, 4422–4432.
39. Kim, C. K.; Kim, T.; Choi, I. Y.; Soh, M.; Kim, D.; Kim, Y. J.; Jang, H.; Yang, H. S.; Kim, J. Y.; Park, H. K.; *et al*. Ceria Nanoparticles That Can Protect against Ischemic Stroke. *Angew. Chem., Int. Ed.* **2012**, *51*, 11039–11043.
40. Carlson, A.; Bowen, A. M.; Huang, Y.; Nuzzo, R. G.; Rogers, J. A. Transfer Printing Techniques for Materials Assembly and Micro/Nanodevice Fabrication. *Adv. Mater.* **2012**, *24*, 5284–5318.
41. Feng, X.; Meitl, M. A.; Bowen, A. M.; Huang, Y.; Nuzzo, R. G.; Rogers, J. A. Competing Fracture in Kinetically Controlled Transfer Printing. *Langmuir* **2007**, *23*, 12555–12560.

42. Nayak, T. R.; Andersen, H.; Makam, V. S.; Khaw, C.; Bae, S.; Xu, X.; Ee, P. L.; Ahn, J. H.; Hong, B. H.; Pastorin, G.; *et al*. Graphene for Controlled and Accelerated Osteogenic Differentiation of Human Mesenchymal Stem Cells. *ACS Nano* **2011**, *5*, 4670–4678.
43. Wang, L.; Sun, B.; Ziemer, K. S.; Barabino, G. A.; Carrier, R. L. Chemical and Physical Modifications to Poly-(dimethylsiloxane) Surfaces Affect Adhesion of Caco-2 Cells. *J. Biomed. Mater. Res., Part A* **2010**, *93A*, 1260–1271.
44. Webb, R. C. Smooth Muscle Contraction and Relaxation. *Adv. Physiol. Ed.* **2003**, *27*, 201–206.
45. Kim, S. J.; Jun, I.; Kim, D. W.; Lee, Y. B.; Lee, Y. J.; Lee, J. H.; Park, K. D.; Park, H.; Shin, H. Rapid Transfer of Endothelial Cell Sheet Using a Thermosensitive Hydrogel and Its Effect on Therapeutic Angiogenesis. *Biomacromolecules* **2013**, *14*, 4309–4319.
46. Kim, D. W.; Jun, I.; Lee, T. J.; Lee, J. H.; Lee, Y. J.; Jang, H. K.; Kang, S.; Park, K. D.; Cho, S. W.; Kim, B. S.; *et al*. Therapeutic Angiogenesis by a Myoblast Layer Harvested by Tissue Transfer Printing from Cell-Adhesive, Thermosensitive Hydrogels. *Biomaterials* **2013**, *34*, 8258–8268.
47. Juhasa, M.; Engelmayr, C. G.; Fontanella, N. A.; Palmerb, M. G.; Bursac, N. Biomimetic Engineered Muscle with Capacity for Vascular Integration and Functional Maturation *in Vivo*. *Proc. Natl. Acad. Sci. U.S.A.* **2014**, *15*, 5508–5513.
48. Sekine, H.; Shimizu, T.; Sakaguchi, K.; Dobashi, I.; Wada, M.; Yamato, M.; Kobayashi, E.; Umezu, M.; Okano, T. *In Vitro* Fabrication of Functional Three-Dimensional Tissues with Perfusable Blood Vessels. *Nat. Commun*. **2013**, *4*, 1399.
49. Shweiki, D.; Itin, A.; Soffer, D.; Keshet, E. Vascular Endothelial Growth-Factor Induced by Hypoxia May Mediate Hypoxia-Initiated Angiogenesis. *Nature* **1992**, *359*, 843–845.
50. Levenberg, S.; Rouwkema, J.; Macdonald, M.; Garfein, E. S.; Kohane, D. S.; Darland, D. C.; Marini, R.; van Blitterswijk, C. A.; Mulligan, R. C.; D'Amore, P. A.; *et al*. Engineering Vascularized Skeletal Muscle Tissue. *Nat. Biotechnol.* **2005**, *23*, 879–884.
51. van Velthoven, C. T.; Kavelaars, A.; van Bel, F.; Heijnen, C. J. Mesenchymal Stem Cell Treatment after Neonatal Hypoxic-Ischemic Brain Injury Improves Behavioral Outcome and Induces Neuronal and Oligodendrocyte Regeneration. *Brain Behav. Immun.* **2010**, *24*, 387–393.
52. Bae, S.; Kim, H.; Lee, Y.; Xu, X.; Park, J. S.; Zheng, Y.; Balakrishnan, J.; Lei, T.; Kim, H. R.; Song, Y. I.; *et al*. Roll-to-Roll Production of 30-inch Graphene Films for Transparent Electrodes. *Nat. Nanotechnol.* **2010**, *5*, 574–578.

Supporting Information for

Multifunctional cell-culture-platform for aligned cell sheet monitoring, transfer printing, and therapy

Seok Joo Kim[†,‡,#], Hye Rim Cho[†,§,#], Kyoung Won Cho[†,‡,#], Shutao Qiao[⊥], Jung Soo Rhim[∥], Min Soh[†,‡], Taeho Kim[†,‡], Moon Kee Choi[†,‡], Changsoon Choi[†,‡], Inhyuk Park[†,‡], Nathaniel S. Hwang[‡], Taeghwan Hyeon[†,‡], Seung Hong Choi[†,§,*], Nanshu Lu[⊥,*], Dae-Hyeong Kim[†,‡,*]

[†]*Center for Nanoparticle Research, Institute for Basic Science (IBS), Seoul 151-742, Republic of Korea*

[‡]*School of Chemical and Biological Engineering, Institute of Chemical Processes, Seoul National University, Seoul 151-742, Republic of Korea*

[§]*Department of Radiology, Seoul National University College of Medicine, Seoul 110-744, Republic of Korea*

[⊥]*Center for Mechanics of Solids, Structures, and Materials, Department of Aerospace Engineering and Engineering Mechanics, Texas Materials Institute, University of Texas at Austin, 210 E 24th Street, Austin, Texas 78712, USA*

[∥]*School of Mechanical and Aerospace Engineering, Seoul National University, Seoul 151-742, Republic of Korea*

[#]*S. J. Kim, H. R. Cho and K. W. Cho contributed equally to this work.*

*Address correspondence to *dkim98@snu.ac.kr*, *nanshulu@utexas.edu*, *verocay@snuh.org*

This Supporting information contains:

Text, Table, and Figures

1. Text

1.1. FEM and analytical modeling of energy release rate vs. crack length

Abaqus 6.10 is used to perform finite element modeling (FEM) to study the relation between energy release rate and crack length when peeling a soft PDMS film from a glass substrate as shown in Figure S9a in the Supporting Information. We simplify the problem to be 2-dimensional plane strain and the boundary conditions we applied are: i) the bottom of the glass slide is fixed; ii) the left edge of the PDMS film is loaded by either fix force F or fix deflection Δ, for different crack size a. The PDMS film is modeled as Neo-Hookean material while the glass slide is treated as elastic material and their mechanical properties as well as geometries are shown in Table S1 in Supporting Information. The crack is defined as a seam with length a on the PDMS/Glass interface (the red solid line in Figure S9a in the Supporting Information) and near the crack front an integral path (the yellow circular path in the zoomed in picture in Figure S9a in the Supporting Information) is assigned for the J-integral to obtain the energy release rate at the crack tip. Path independence of the J-integral has been checked and ensured. The overall structure is meshed by quadratic quadrangle CPE8RH element except near the crack tip (quadratic triangular CPE8RH element) and the results are plotted in Figure S9b in the Supporting Information by solid circular dots for both force control under F_1 = 0.01 N/m (blue) and F_2 = 0.02 N/m (red) and displacement control under Δ_1 = 300 μm (blue) and Δ_2 = 600 μm (red).

Since the glass is much stiffer compared to the PDMS, analytical approximations can be made by neglecting the deformation of the glass slide and treating the debonded part

of the PDMS film as a cantilever beam (of length a) undergoing small deflection due to the applied loadings (F or Δ). Then the total strain energy U can be expressed as

$$U = \frac{F^2 a^3}{6\bar{E}I} = \frac{3\Delta^2 \bar{E}I}{2a^3} \qquad \text{(S1)}$$

where $\bar{E}I$ is the bending rigidity of the PDMS film and

$$\frac{F}{\Delta} = \frac{3\bar{E}I}{a^3} \qquad \text{(S2)}$$

Thus, the energy release rate is

$$G = \left(\frac{\partial U}{b\partial a}\right)_F = \frac{\partial}{b\partial a}\left(\frac{F^2 a^3}{6\bar{E}I}\right) = \frac{F^2 a^2}{2\bar{E}I} \qquad \text{(S3)}$$

for force control and

$$G = \left(-\frac{\partial U}{b\partial a}\right)_\Delta = -\frac{\partial}{b\partial a}\left(\frac{3\Delta^2 \bar{E}I}{2a^3}\right) = \frac{9\Delta^2 \bar{E}I}{2a^4} \qquad \text{(S4)}$$

for displacement control where b is the out of plane thickness for the bilayer structure and is set to be unit length for the plane strain problem. These analytical approximations are plotted as solid curves in Figure S9b in the Supporting Information which compares favorably with the FEM results. It is noticed that under force control, the energy release rate increases monotonically with both force and crack length, which serves as the foundation of our explanations for cell sheet transfer given in Figure 5.

1.2. Effect of PDMS margin size

PDMS margin size, which is defined as the distance between the edge of graphene and the edge of PDMS, is experimentally found to be a significant control parameter on the yield of cell sheet transfer printing, as shown in the right frame of Figure 5f. It is observed that the transfer yield is lower than 40% when there is no margin, *i.e.* when the whole surface of the PDMS is covered by graphene and cell sheet. In our fracture mechanics model, we

assume that only cell sheets are adhered to polystyrene, hence bare PDMS to polystyrene contact zone is considered as the initial interface crack and therefore the margin size is the initial crack size. The stress state at the edge of the cell sheet looks very different when there is or is not margin, as shown in Figure S10 in the Supporting Information. FEM is applied via Abaqus 6.10 and results are plotted in Figure S10b in the Supporting Information as solid circular dots for different margin size: 0 μm (blue), 500 μm (red) and 1000 μm (green). As we can see from Figure S10b in the Supporting Information, larger margin size does give us higher normal stretching stresses near the edge of cell sheet when peeling the PDMS off polystyrene, which leads to a larger damaged cell zone, and hence larger effective crack size. Figure S10c in the Supporting Information offers the contour plots of the stress field for different margin sizes. Higher stress is found when the margin size is larger.

1.3. Effect of cell sheet moisture

Water can migrate through cell sheet due to capillary effect and then wet the graphene/cell interface such that the adhesion of graphene/cell can be reduced,[1] *e.g.* from $\Gamma'_{C/Graph}$ to $\Gamma_{C/Graph}$ in Figure S11b in the Supporting Information. The critical forces for PDMS/graphene and cell/graphene interfacial cracks to propagate are represented by F_3 and F_2, respectively. After moisture added in between of graphene and cell sheet, the previously stronger adhesion $\Gamma'_{C/Graph}$ ($\Gamma'_{C/Graph} > \Gamma_{PDMS/Graph}$) now becomes the weaker one ($\Gamma_{C/Graph} < \Gamma_{PDMS/Graph}$) such that the critical force for cell/graphene crack propagation is smaller than that of PDMS/graphene ($F_2 < F_1$). Thus, when peel PDMS off

the wet sample, graphene remains attached on PDMS, as illustrated by Figure S11c in the Supporting Information.

1.4. Effect of cell sheet continuity

For discontinuous cell sheet, though stretching effect can still be induced in preparation step, due to the existence of the gaps in between of neighboring cell islands, the stretching effect of the cell can be relaxed and such that the shear-induced crack size is not as significant as that of continuous cell sheet (see Figure S12a in the Supporting Information). With $\Gamma_{C/Graph}$ and $\Gamma_{C/Glass}$ unchanged, a larger force is needed to initiate crack propagation for cell/graphene interface (F_2) than that for cell/glass interface (F_1) as shown in Figure S12b in the Supporting Information, which means, when quasi-statically increasing the applied force F, the crack of the cell/glass interface begins to propagate first, *i.e.* sample will stay with graphene and be peeled off from glass.

Reference

1. Kasemo, B. Biological surface science. *Surf. Sci.* **2002,** *500*, 656-677.

2. Table

Table S1. Properties of the PDMS film and the glass slide

	Young's Modulus	Poisson's Ratio	Thickness (μm)	Material Model
PDMS	36 KPa	0.49	500	Neo-Hookean
Glass	70 GPa	0.3	1000	Linear Elastic

3. Figures

See next pages.

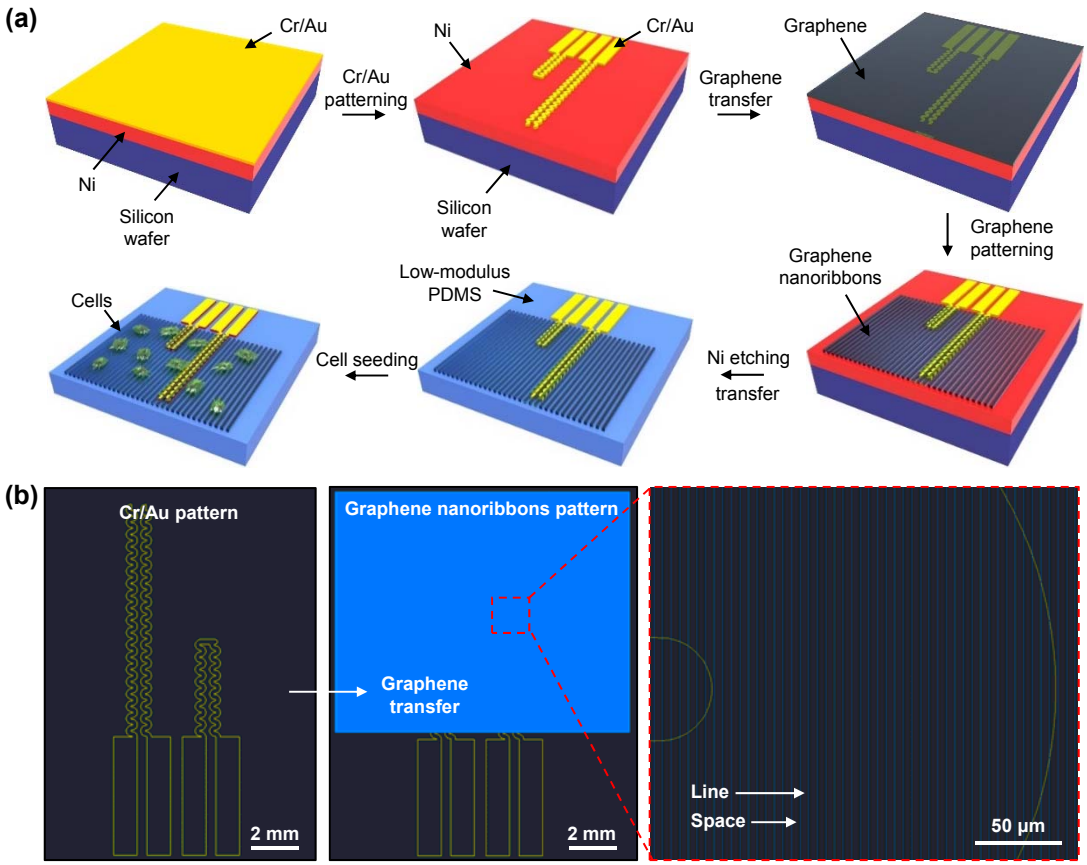

Figure S1. Detailed fabrication process of the stretchable instrumented cell-culture-platform. (a) A schematic overview of the fabrication process. (b) AutoCAD designs of impedance and temperature sensors, along with the patterned graphene nanoribbons.

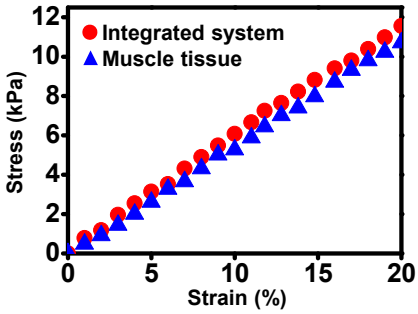

Figure S2. Stress-strain curve for system modulus of integrated system and muscle tissue.

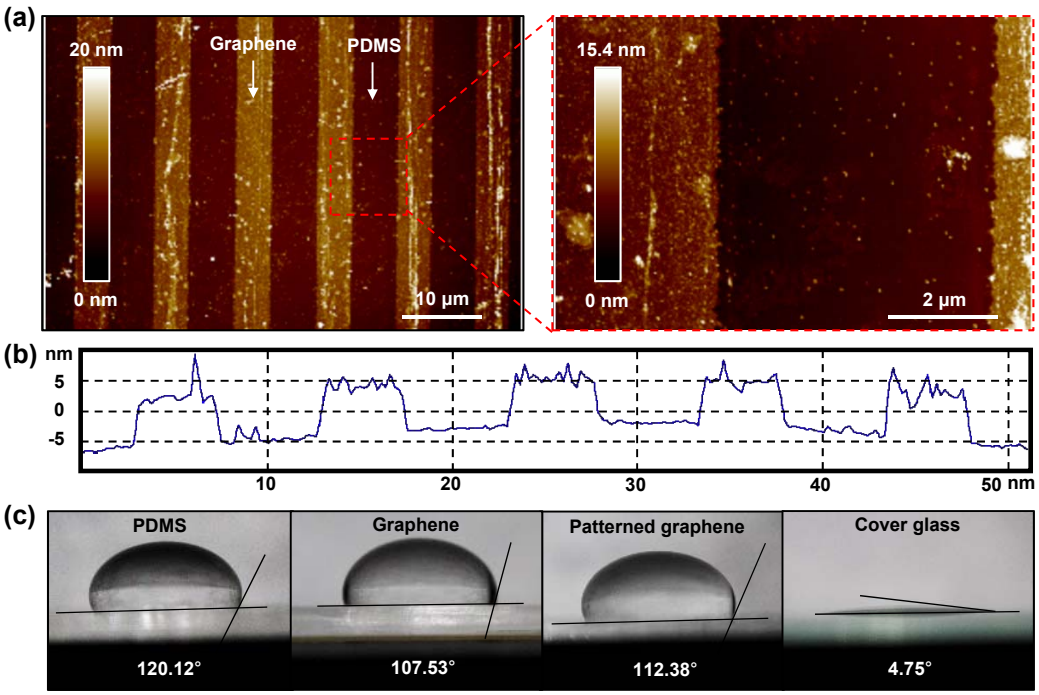

Figure S3. Characterization of patterned graphene nanoribbons. (a) AFM topological image of the patterned graphene on PDMS. Spring constants of cantilevers (TESP, Bruker probes) is 42 N/m and all AFM data are measured with a tapping mode. Data are visualized by the NanoScope Analysis software (Bruker). (b) AFM topological graph of patterned graphene on PDMS. (c) Water contact angles of various substrates: PDMS, graphene, patterned graphene (widths of line and spacing; 5 μm), and cover glass.

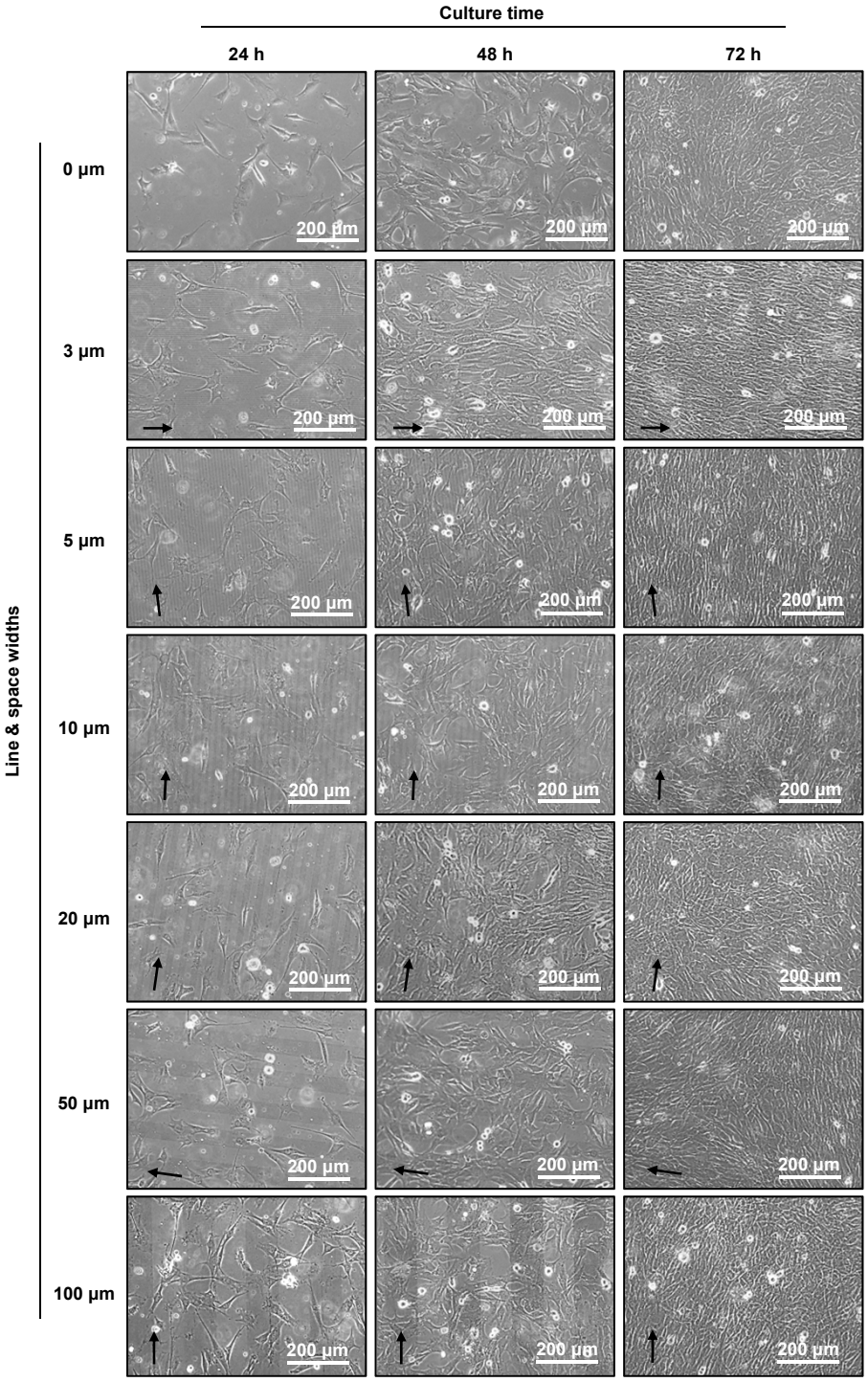

Figure S4. Phase-contrast microscope images of cell alignments in respect to pattern sizes and culture time. C2C12 myoblasts are cultured on the 7 different graphene patterns with different line and space widths (0, 3, 5, 10, 20, 50, and 100 μm) to find the best pattern width for cell alignments. Each sample is observed at three different time (24, 48, and 72 h after the culture) by the phase-contrast microscopy.

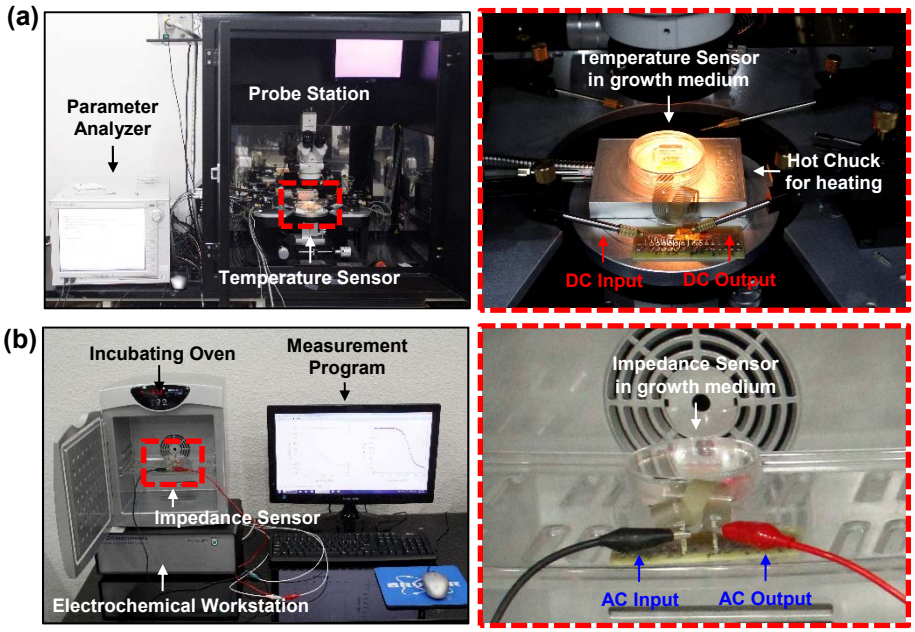

Figure S5. Images of experimental setups for the sensor characterization. (a) Characterization of the temperature sensor in the growth medium by the probe station and parameter analyzer. For heating, the sensor is placed on a hot chuck. (b) Characterization of the impedance sensor in the growth medium by the electrochemical workstation while maintaining its environment temperature as 37 °C in an incubating oven.

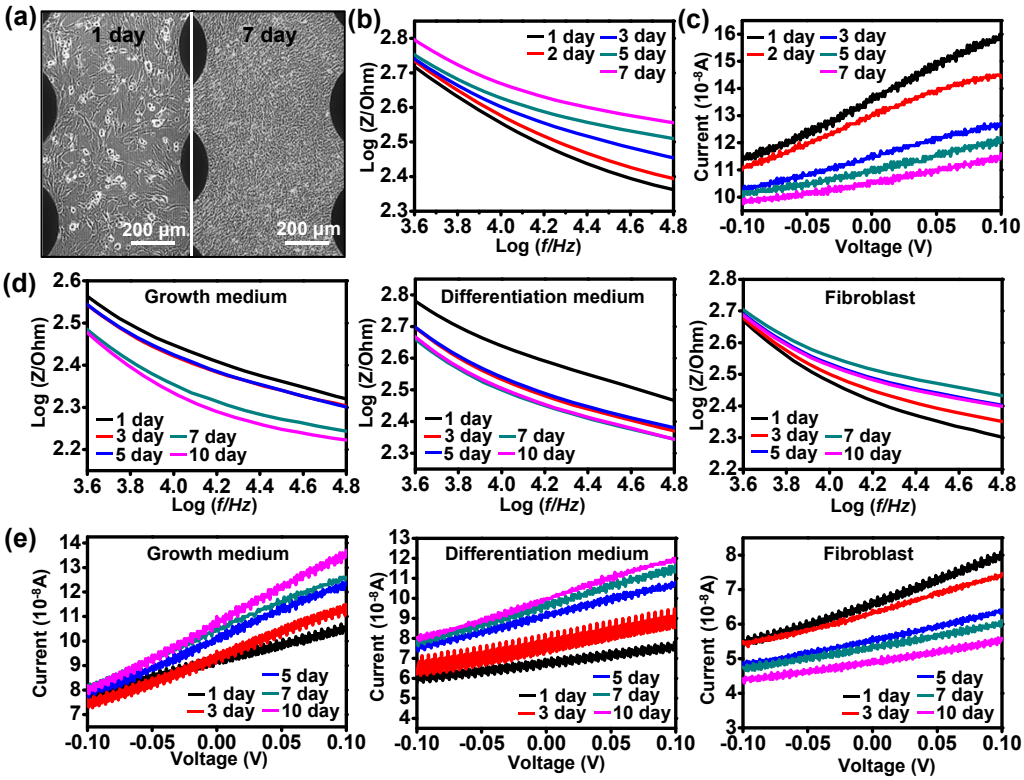

Figure S6. Impedance change during proliferation and differentiation of C2C12 myoblasts. (a) Phase contrast microscope images of C2C12 myoblasts proliferating on the instrumented cell-culture-platform after 1 and 7 days of culture. Time-dependent changes of (b) impedance and (c) I-V curve as the C2C12 myoblasts proliferate. (d) Time-dependent impedance change during the differentiation of C2C12 myoblasts cultured in the growth medium (left) and differentiation medium (middle). The right frame shows the impedance change of fibroblast in the growth medium (control). (e) Time-dependent I-V curve changes during the differentiation of C2C12 myoblasts cultured in the growth medium (left), and differentiation medium (middle). The right frame shows the I-V curve change of fibroblast in growth medium (control).

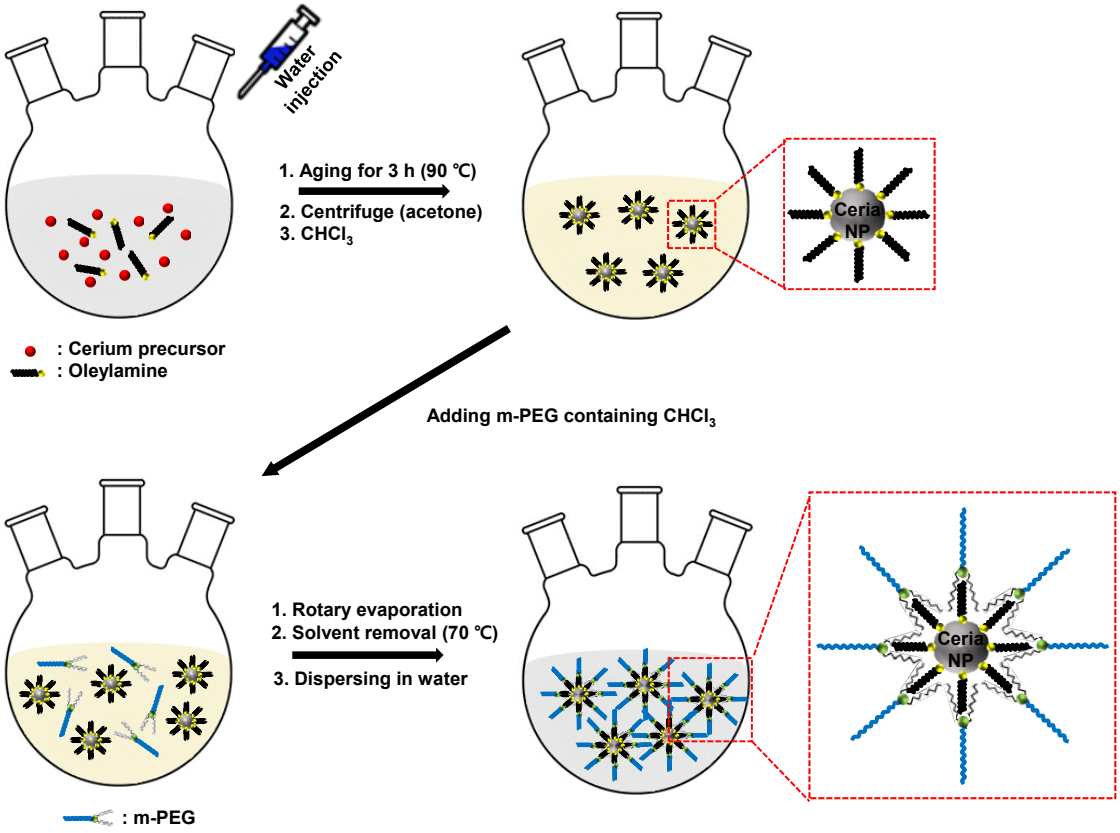

Figure S7. A schematic overview of the synthesis process of ceria nanoparticles.

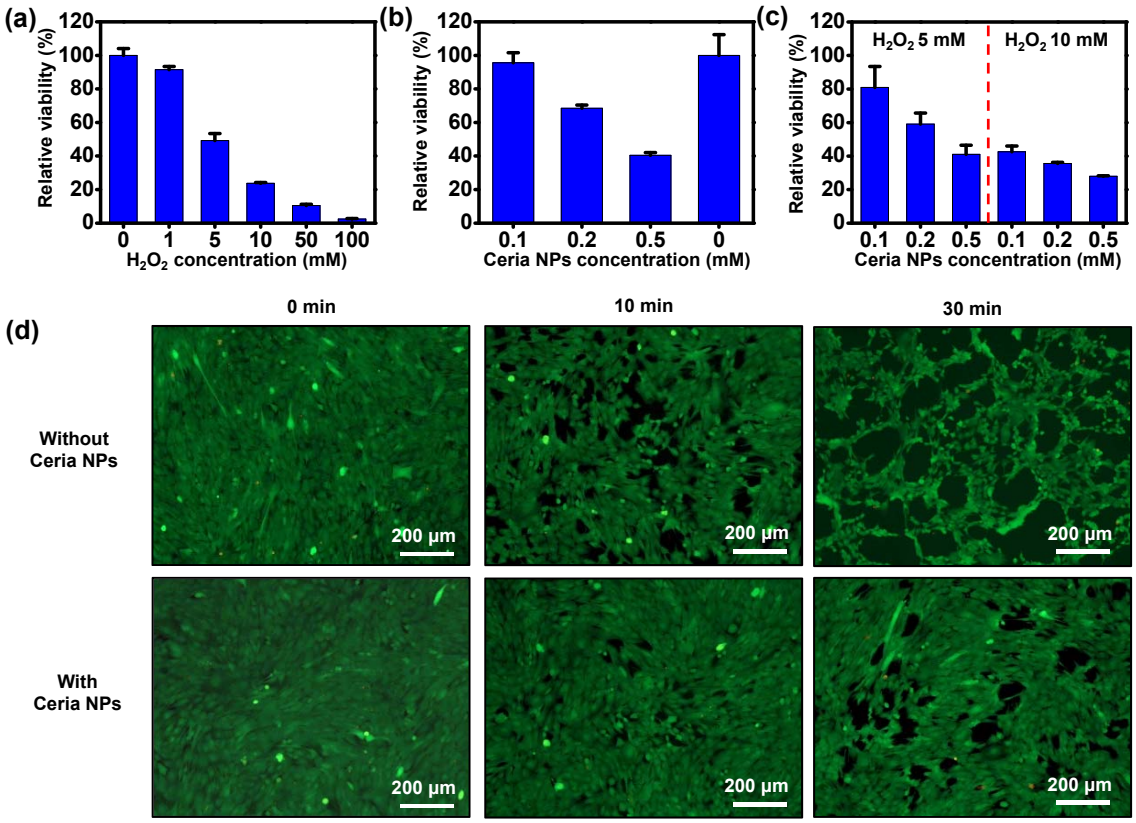

Figure S8. Effects of ceria nanoparticles on cellular viability. A plot of relative viability of cells depending on the concentration of (a) hydrogen peroxide (H_2O_2) and (b) ceria nanoparticles (Ceria NPs). (c) A graph of relative viability of cells versus concentrations of Ceria NPs with 5 mM and 10 mM of H_2O_2 treatments. All data are acquired after treating H_2O_2 and Ceria NPs for 30 min, then the samples are incubated in the MTT solution (Amresco) for 3 h. Data are quantified by using a microplate reader (SpectraMax M3, Moelcular Devices). (d) Fluorescence images of H_2O_2-exposed C2C12 cells with/without Ceria NPs at different time periods. H_2O_2-exposed cells with/without Ceria NPs are stained with LIVE/DEAD Viability Kit and observed by a fluorescence microscopy.

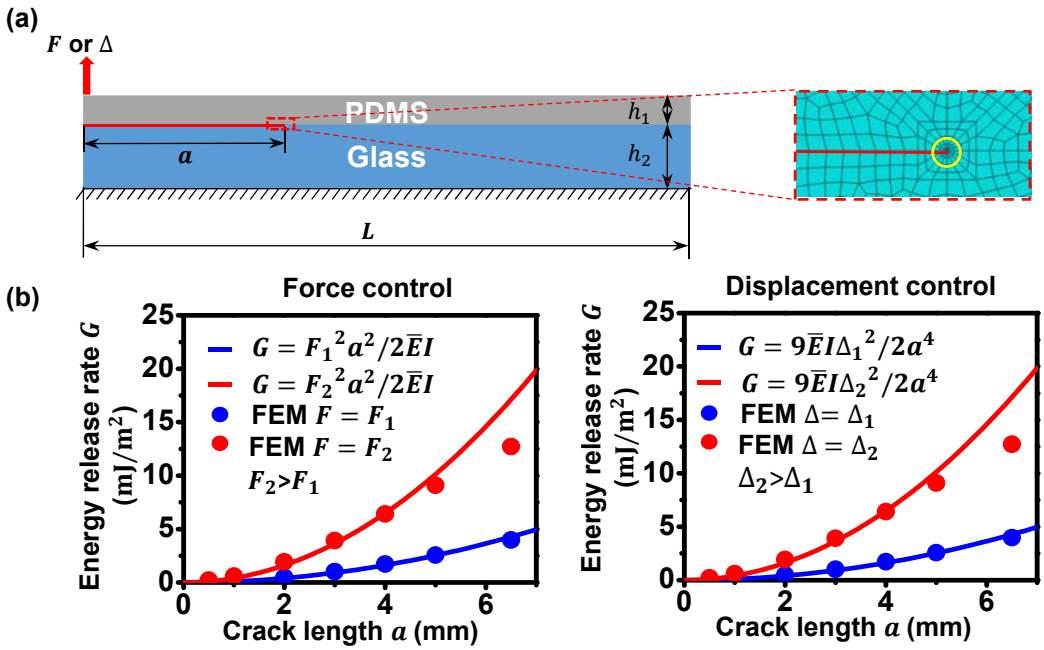

Figure S9. Theoretical analysis for crack propagation in cell sheet. (a) FEM simulation of PDMS/Glass interfacial crack under force control (F) or displacement control (Δ). (b) Comparison of $G \sim a$ relations between the FEM results (dots) and the analytical approximations (curves) for both the force control under F_1 = 0.01 N/m (blue) and F_2 = 0.02 N/m (red) and the displacement control under Δ_1 = 300 μm (blue) and Δ_2 = 600 μm (red).

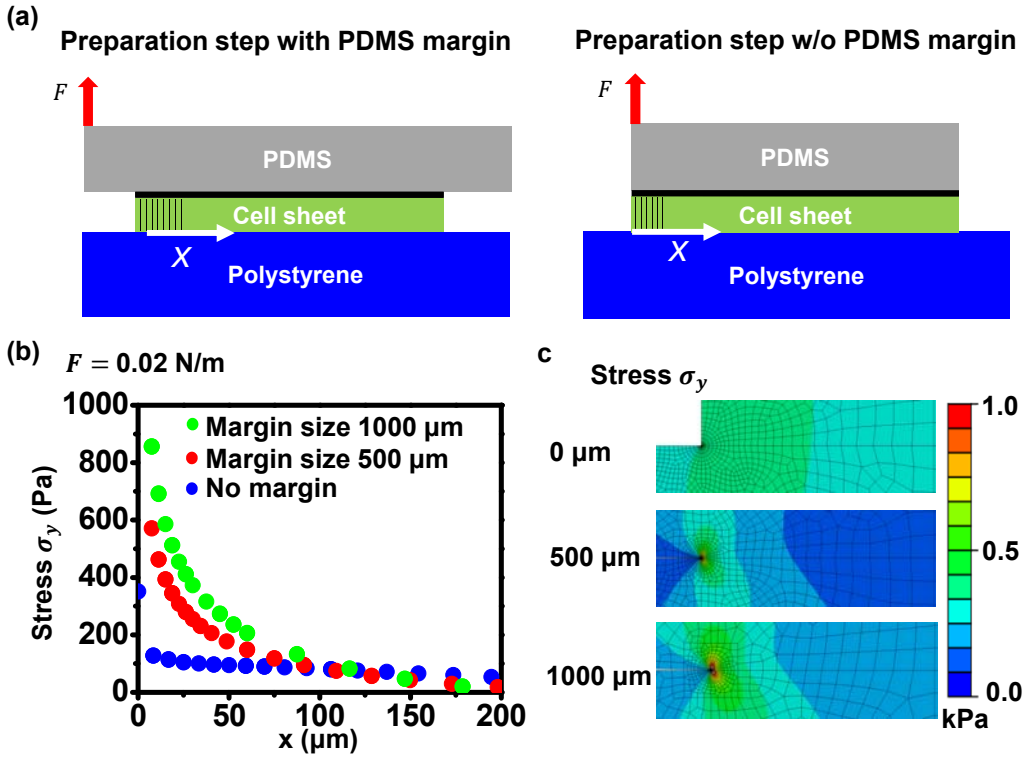

Figure S10. Theoretical analysis for the effect of PDMS margin on cell sheet transfer printing. (a) Schematic images for the preparation step with or without PDMS margin. (b) Comparison of the FEM results (solid circular dots) of the stress (σ_y) distributions along the cell/PS interface between different margin sizes: 0 μm (blue), 500 μm (red) and 1000 μm (green). Axis x is shown in (a) pointing along the interfacial direction and axis y is in the perpendicular direction of axis x. The force applied in the 2D FEM model is 0.02 N/m. (c) FEM contour plot of stress distribution (σ_y) near the cell sheet edge for different margin sizes: 0 μm, 500 μm and 1000 μm.

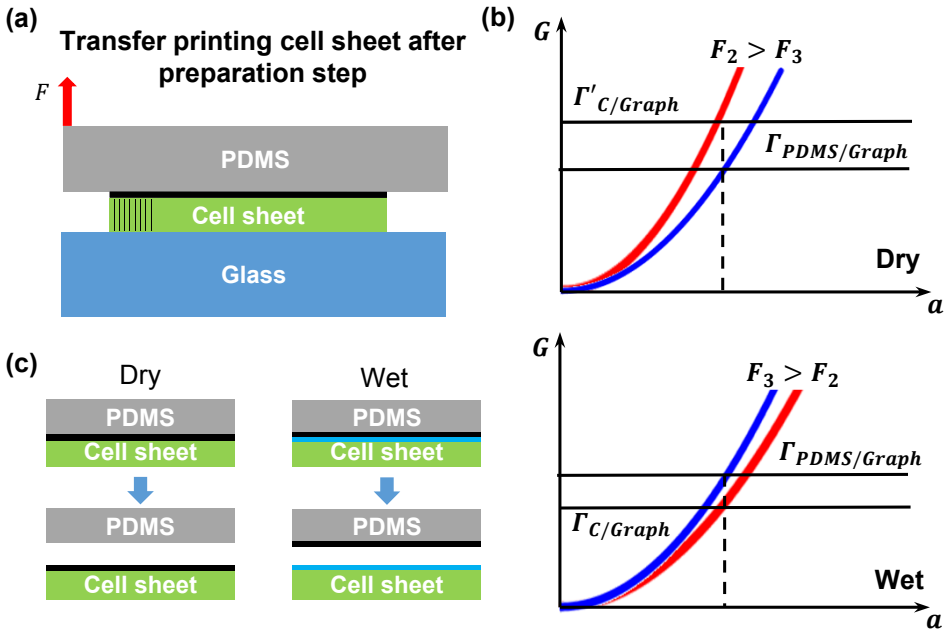

Figure S11. Theoretical analysis for the effect of moisture on cell sheet transfer printing. (a) Schematic image of transfer printing cell sheet after preparation step. (b) Moisture is considered to be a factor that reduces the adhesion of cell/graphene interface which lower the critical force needed for crack of cell/graphene interface to propagate. (c) After transferring, the graphene layer remains on the cell sheet for dry samples but stays with PDMS for wet samples.

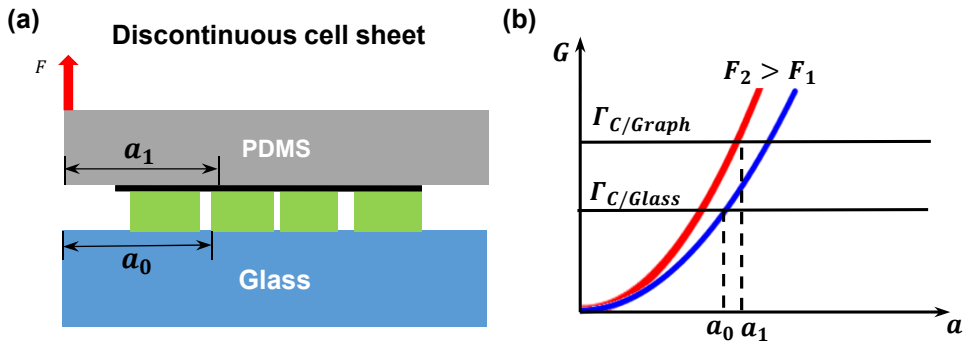

Figure S12. Theoretical analysis for the effect of cell sheet continuity on transfer printing. (a) Schematic image of a sample with discontinuous cell sheet on glass after preparation step. The sizes of cell/glass crack and effective cell/graphene interface crack are denoted by a_0 and a_1, respectively. (b) Due to the relaxation of gaps between neighboring cell islands, the stretch induced increase of the crack length of cell/PDMS interface is not significant. Thus, though a_1 is greater than a_0, the critical force for crack propagation of cell/graphene interface is larger than that of cell/glass interface ($F_2 > F_1$), i.e. crack propagation will firstly happen on cell/glass interface.

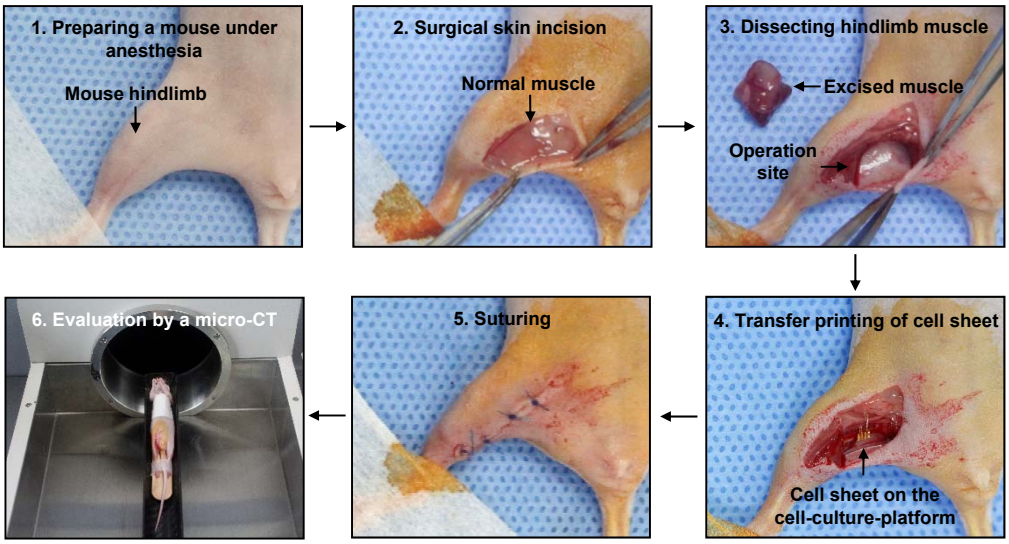

Figure S13. Images of surgery and cell sheet transfer-printing in the scarred muscle model of a mouse.

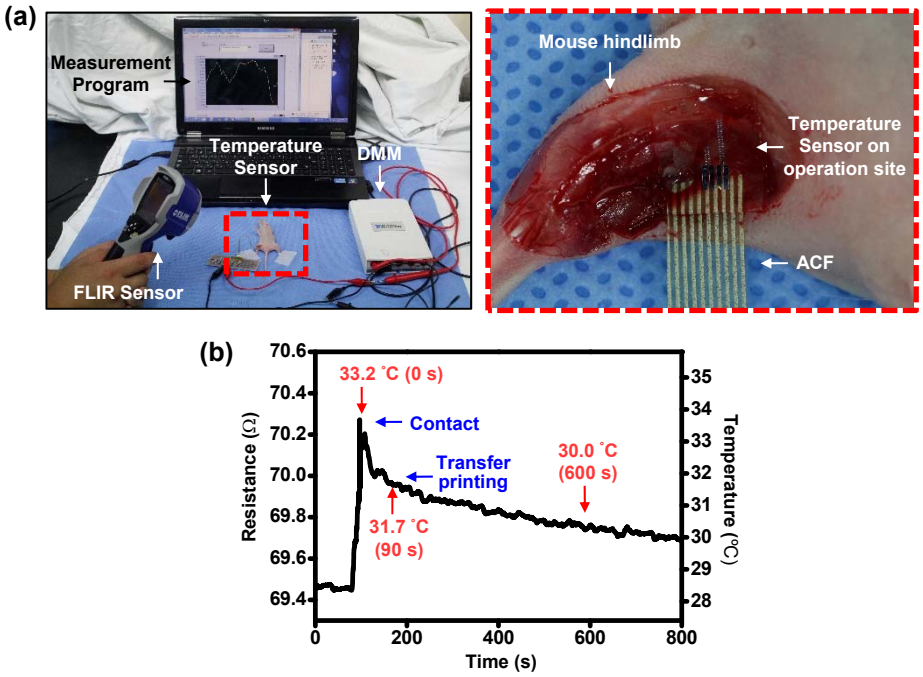

Figure S14. Measurement of temperature change with the instrumented cell-culture-platform during transfer-printing of the cell sheet *in vivo*. (a) Images of the temperature sensing experiment. After dissecting muscle, the ACF-connected instrumented cell-culture-platform is placed on the operation site. Then, the time-dependent resistance change of the temperature sensor is measured over 10 min with a Digital Multimeters (DMM, National Instrument) and the data is plotted in (b). The time-dependent temperature is also measured simultaneously by the commercial optical thermometer which is indicated by red arrows.

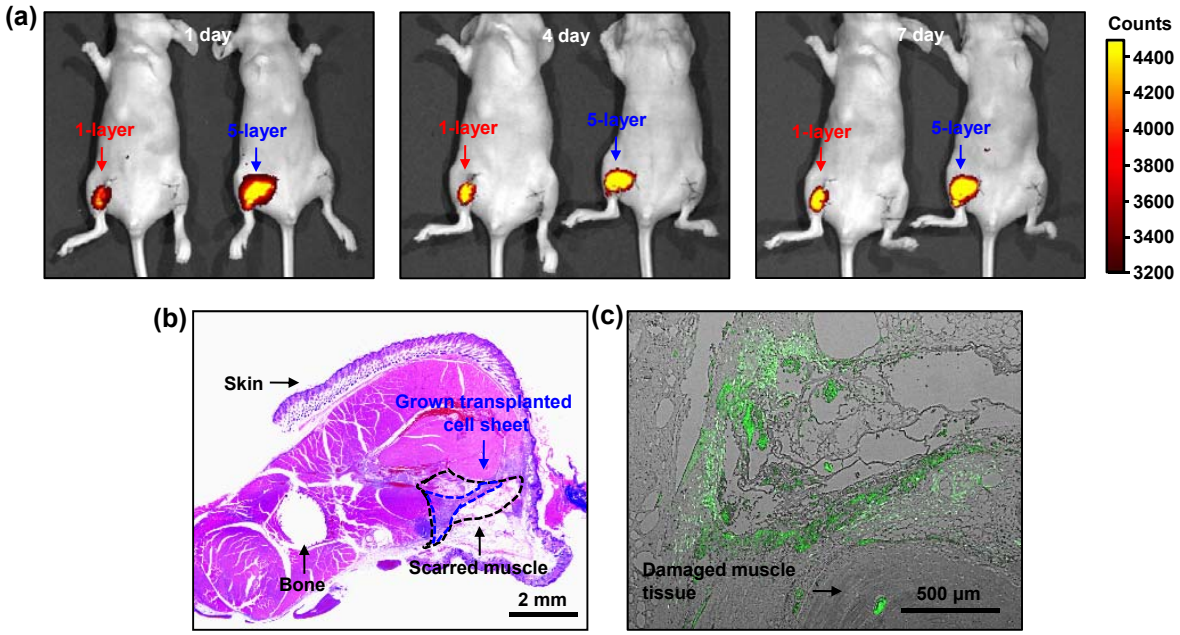

Figure S15. The fluorescence images and histological analysis of mice transplanted with cell sheet. (a) The fluorescence images show that both 1-layer and 5-layer of transplanted cell sheets maintain their structure and original location for over 7 days. (b) Image of H&E staining and (c) fluorescence image of the transplanted cell sheet expressing GFP for histological analysis of the monolayer cell sheet transplanted at the scarred region.

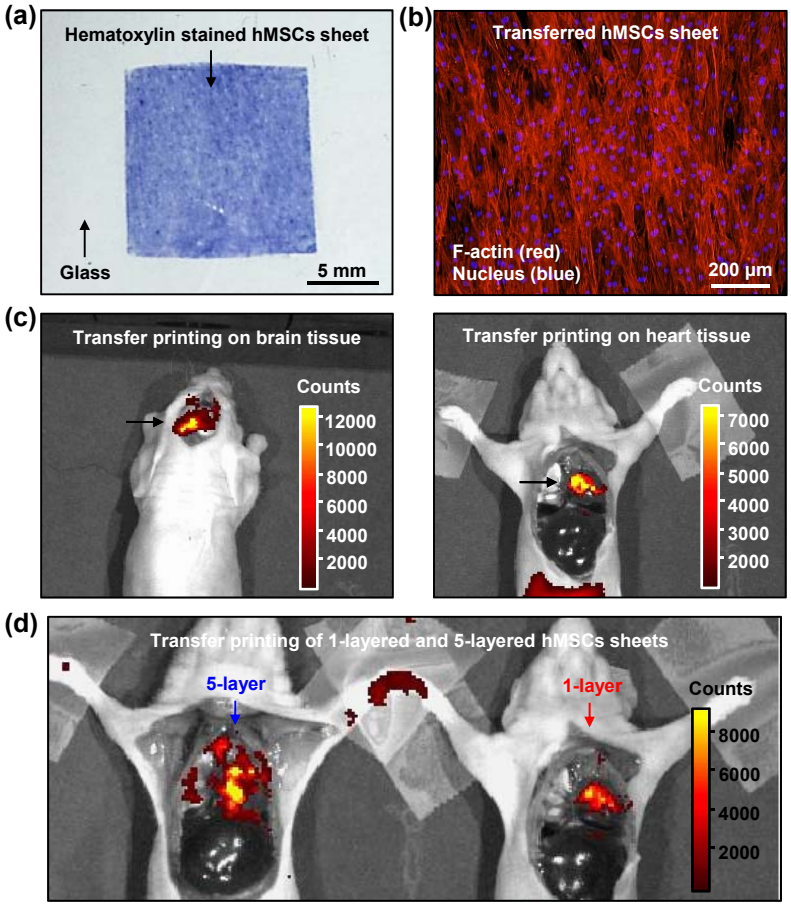

Figure S16. Transfer printing of hMSCs sheet. (a) Observation of hMSCs sheet after transfer printing onto the protein coated glass by staining the cells with hematoxylin. (b) The maintenance of cytoskeletal organization of hMSCs sheet after transfer printing on the glass. (c) The fluorescence images of the hMSCs sheet transfer-printed onto brain (left) and heart (right) tissues. For cell sheet transplantation, brain and heart of anesthetized mice are exposed by surgery. (d) The fluorescence image of the multiple transfer printings of hMSCs sheets (five sheets in total) onto the heart tissues. Left and right show experimental and control image, respectively.